



Neural network-based variable stiffness impedance control for internal/external forces tracking of dual-arm manipulators under uncertainties

Yufei Zhou^{a,b}, Zhongcan Li^{a,b}, Yanhui Li^a, Mingchao Zhu^{a,*}

^a ChangChun Institute of Optics, Fine Mechanics and Physics, Chinese Academy of Sciences, Changchun, 130033, China

^b University of Chinese Academy of Sciences, Beijing, 100049, China

ARTICLE INFO

Keywords:

Dual-arm manipulators
Variable stiffness impedance control
Internal force-tracking
Geometry and stiffness uncertainties

ABSTRACT

The desired interaction between manipulators, objects, and environments has resulted in the internal/external force control for dual-arm manipulators being in increasing demand. Consequently, this study focused on the internal/external force tracking for dual-arm manipulator systems under external disturbances, geometries, and stiffness uncertainties which continuously lead to unsatisfactory internal force tracking. The proposed scheme is based on a two-level adaptive impedance control scheme, where the stiffness coefficient is adjusted to adapt to uncalibrated objects. An object-level hybrid impedance controller was used to regulate the external disturbance to produce a compliant response. A manipulator-level neural network-based variable stiffness impedance controller (NNVSIC) was proposed to regulate the internal force under various uncertainties. Additionally, an adaptive wavelet neural network was designed to compensate for the geometric estimation errors of the object. The variable stiffness coefficient could automatically adapt to an unknown object during the cooperation process. One advantage of the proposed method is that no prior knowledge was required. The same controller parameters could be adapted to various objects. The asymptotic stability of the proposed NNVSIC was proven via Lyapunov stability analysis. A series of experiments were conducted using two self-developed nine-degrees-of-freedom redundant manipulators. Furthermore, hard and soft objects of various geometries and stiffnesses were used to verify the effectiveness of the algorithm. The experimental results demonstrated the efficiency and superiority of the proposed controller through performance comparison with various algorithms.

1. Introduction

Robots have been widely used in the cleaning (Kim, Yoo, Seo, Kim, & Kim, 2020), machining (Zhao, Tao, & Qian, 2020), assembling (Kang, Yi, Song, & Yi, 2021), and polishing (Ochoa & Cortesao, 2021; Wahballa, Duan, & Dai, 2022) fields, amongst many others (Rani, Kumar, & Singh, 2019). In applications where a single robot may not be able to perform a task in the desired manner, coordination between multiple manipulators is required. Compared with a single manipulator, a multi-manipulator system offers greater flexibility, manipulability, load capacity (Kim, Balakirsky, Ahlin, et al., 2021), and workspace (Smith, Karayiannidis, Nalpantidis, et al., 2012). However, a dual-arm system has twice as many joints to control as a single manipulator, making the system model and controllers of dual-arm manipulator systems more complex than those of single manipulators.

The kinematics of two manipulators gripping a common object can be modeled as a closed-chain system with constraints; many studies

having investigated control methods for nonlinear constrained systems (Sun, Song, Song, et al., 2023; Tao, Qiu, Chen, et al., 2023; Zhou, Tao, Chen, et al., 2022). To coordinate the movements of dual-arm manipulators, Liu, Lei, Han, et al. (2016) proposed three levels of motion control methods to decompose the motion of an object, the kinematic position of the manipulators being solved using a closed-chain constraint relationship. Lee, Chang, and Jamisola (2013) proposed a relative Jacobian technique to determine the motion position of two manipulators. Compared with single-arm systems, dual-arm manipulators could experience load or force distribution problems between the two manipulators and the object. Here, the force exerted on objects could be decomposed into motion-inducing and internal forces. To solve this problem, Chung, Yi, and Kim (2005) proposed the Moore–Penrose inverse of the grasp matrix, the internal force being calculated by null-space decomposition (Erhart & Hirche, 2015). Consequently,

* Corresponding author.

E-mail addresses: zhoyufei20@mails.ucas.ac.cn (Y. Zhou), lizhongcan20@mails.ucas.ac.cn (Z. Li), liyanhui-1986@163.com (Y. Li), mingchaozhu@gmail.com (M. Zhu).

<https://doi.org/10.1016/j.conengprac.2023.105714>

Received 21 March 2023; Received in revised form 27 August 2023; Accepted 14 September 2023

Available online 4 October 2023

0967-0661/© 2023 Elsevier Ltd. All rights reserved.

the aforementioned force-distribution scheme has been widely applied in the field of dual-arm cooperation.

Difficulties in force control during dual-arm cooperation have been consistently problematic in recent years. The first challenge has been to control the contact behavior between the manipulated object and the environment, referred to as external force control. Another challenge has been to reliably control the handling force and moment exerted on manipulated objects, the difficulty of external force control being that the environment is typically dynamic and uncalibrated. Owing to the existence of environment position estimation errors, the environment position compensation control law (Jung, Hsia, & Bonitz, 2004) and variable damping impedance controller (Dong, Xu, Zhou, et al., 2020; Duan, Gan, Chen, et al., 2018) have been proposed to compensate for position and stiffness uncertainties. Based on the aforementioned research, the adaptive hybrid impedance controller (HIC) (Cao, He, Chen, et al., 2020; Sheng & Zhang, 2018) was proposed to solve the dynamic contact force-tracking problem. The aforementioned methods compensated for uncertainties by adjusting the impedance parameters, whereas other methods adjusted the reference trajectory. Jung and Hsia (2000a) and Zhang and Khamesee (2017) proposed a model reference adaptive control law to update the reference trajectory. Additionally, Seraji and Colbaugh (1997) proposed an adaptive law based on the feedback force to estimate the environmental stiffness and position, this scheme utilizing the estimated environmental parameters to generate the command position for dynamic contact tracking. However, the aforementioned algorithms did not compare the force-tracking results in environments with various stiffnesses.

All dual-arm manipulator applications normally involve the robot system touching the object. In such scenarios, the internal force must be regulated to prevent physical damage to the robot or object. To date, controllers for coordinating multiple manipulators have generally been classified as master–slave, hybrid position/force, or impedance controllers.

In the master–slave control mode, one of the manipulators is defined as the master whose trajectory and operational force are predetermined. Slave manipulators adjust their trajectories based on the closed-chain constraint and the force distribution equation (Yan, Mu, Xu, et al., 2016). The control performance can be greatly affected by the slave manipulator owing to the uncertainties in the grasp matrix, the asymmetric motion control mode leading to greater object trajectory tracking errors. Moreover, the adjustment speed is slower than that when two master manipulators coordinate together. The hybrid position/force control of an object being manipulated by two coordinated manipulators with rigid grasps has been studied in Aghili (2010), Calanca, Muradore, and Fiorini (2015), Gierlak and Szuster (2017), Gueaieb, Karray, and Al-Sharhan (2007), Mohajerpoor, Rezaei, Talebi, et al. (2012). It comprises two control modes—that is, the position control mode for free spaces and the force control mode for constrained spaces. However, control modes that need to switch between different workspaces can cause the system to oscillate. Consequently, the force control space may require a dynamic model, which can be difficult to obtain.

Impedance control has been widely applied to multi-manipulator systems with promising results (Chen, Guo, Li, et al., 2022; Ferraguti, Landi, Sabattini, et al., 2019). Bonitz and Hsia (1996) first proposed an internal force impedance controller for a dual-arm manipulator system, this approach enforcing a relationship between the internal force and position. To compensate for dynamic trajectory deviations and stiffness uncertainties, Jiao, Yu, Su, et al. (2022) and Hu and Cao (2022) proposed an adaptive impedance controller to adjust the damping parameter. The interaction forces were fed back to the controller to adjust the internal impedance controller parameters. However, although adaptive damping parameters could compensate for errors, the parameter robustness was insufficient because the same controller parameters could not adapt to different objects. To enhance the compliance interaction with the environment, a multilevel impedance control scheme

was developed in Jinjun, Yahui, Ming, et al. (2019) and Sadeghian, Ficuciello, Villani, et al. (2012); a three-level impedance control scheme that included null-space impedance control could establish compliant behavior for dual-arm manipulators, redundant degrees of freedom being used to cope with the joint disturbance. It ensured the execution of the main task while minimizing the influence of external disturbances (Sadeghian, Villani, Keshmiri, et al., 2013). The disadvantage was that null-space impedance control was dependent on precise dynamic models that were difficult to obtain in practice. As such, these methods—that is, variable damping or stiffness—could not guarantee both satisfying external disturbance compliance, internal force control under geometry and stiffness uncertainties, or parameter adaptive robustness.

As nonlinear functions with strong approximation and learning abilities, neural networks (NNs) are widely used in the force control field (Jiang, Wang, Miao, et al., 2020; Nguyen, Thai, Phan, et al., 2019; Tuan, Joo, Tien, et al., 2017). NN-based adaptive controllers can generally be classified into two categories—that is, NN-based controllers that compensate for model uncertainties and NN-based controllers that adaptively adjust the controller parameters. As an example of the first category, Jung and Hsia (2000b) proposed an NN as a compensator to remove all uncertainties, with intelligent impedance control using a wavelet neural network (WNN) realizing force tracking in varying environments (Hamedani, Sadeghian, Zekri, et al., 2021). Guo, Zhang, Celler, and Su (2019) proposed neural adaptive backstepping control to drive the electrohydraulic actuator, with an NN being used to train the unknown model dynamics. Fuzzy NNs are also widely used as uncertain plant model compensators (He & Dong, 2017), hand impedance estimators (Chien, Wang, & Cheng, 2021), unknown model matrix adaptors, and contact environment stiffness parameter estimators (Lee & Wang, 2016). These studies improved the control performance by reducing the system uncertainty. As an example of the second category, Zhang, Cheng, Cao, et al. (2023) used a NN to train variable impedance skills. Zhai, Zhang, Wang, et al. (2022) proposed a two-loop radial basis function (RBF)-NN impedance control for cooperative manipulators. For the robot–environment interaction problem, Zhang, Sun, and Deng (2020) proposed variable impedance parameters to ensure stability. In Panwar, Kumar, Sukavanam, et al. (2012), an adaptive neural controller was designed to regulate the internal force of a multiple robot manipulator system. However, the controller was only simulated and was not experimentally verified. Inspired by Jiao et al. (2022), humans could grasp objects of unknown geometry and stiffness by adjusting the arm stiffness, the adjustment mode not requiring any prior knowledge—that is, the stiffness was adjusted online. This working mode inspired us to use the WNN to adjust the manipulator stiffness online.

In this study, a two-level adaptive impedance control scheme was proposed for the internal/external force tracking of dual-arm manipulators under uncertainties. In practice, uncertain factors—such as external disturbances, geometries, and stiffness uncertainties—always exist. Consequently, an external HIC was used to regulate external disturbances and avoid damage. An neural network-based variable stiffness impedance controller (NNVSIC) could compensate for the above uncertainties and track the required internal force by adjusting the stiffness parameter of the impedance controller. Moreover, unlike other algorithms (Hu & Cao, 2022; Jiao et al., 2022; Jinjun et al., 2019; Sadeghian et al., 2012) that rely on appropriate impedance parameters and adaptive gains, the proposed controller could adapt to objects with different stiffnesses and geometries without modifying the controller parameters.

The main contributions of this paper can be summarized as follows:

- (1) A two-level adaptive impedance control scheme was developed for dual-arm manipulator systems, which includes object-level HIC and manipulator-level NNVSIC. A novel NNVSIC for dual-arm manipulator systems was proposed to achieve internal force tracking under external disturbance, stiffness, and geometry uncertainties. The NN adaptive update law developed could effectively

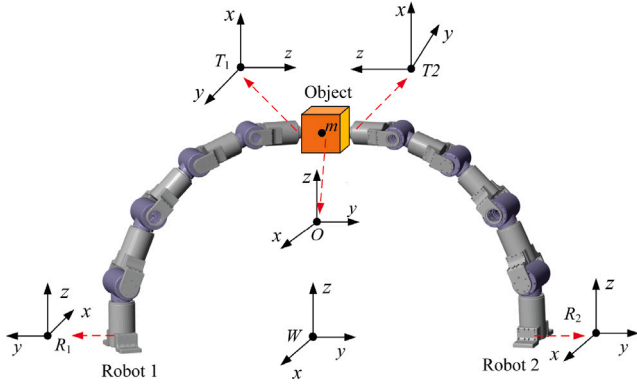


Fig. 1. Coordinate diagram of the dual-arm system.

adjust the robot stiffness parameter online to adapt to unknown objects. Lyapunov stability analysis proved the stability of the controller.

- (2) To demonstrate the effectiveness and superiority of the proposed algorithm, a series of experiments were conducted using two self-developed nine-degrees-of-freedom (9-DOF) redundant manipulators. Objects of different stiffnesses and geometries were manipulated using four different algorithms. The experimental results proved that the proposed controller could effectively realize internal force tracking under uncertainties. Comparisons with various controllers proved the superiority of the proposed algorithm.

The remainder of this paper is organized as follows: The model of the dual-arm manipulator system, force decomposition method, and structure of the WNN are introduced in Section 2. Section 3 presents the NNVSIC. The stability of the NNVSIC is proved using Lyapunov stability analysis in Section 4. The relevant experimental procedures and results are presented in Section 5. Finally, Section 6 summarizes the paper.

2. Theory: Preliminaries

In this section, the dual-arm system model and the WNN structure are introduced. Additionally, the decomposition calculation of the internal/external forces is discussed. Kinematic notations are defined for various coordinate frames that are used in the model derivation. The coordinate diagram of the dual-arm manipulators system is shown in Fig. 1.

- $\{W\}$: World frame;
- $\{R_i\}$: Robot i base frame;
- $\{T_i\}$: Robot i tool frame;
- $\{O\}$: Object frame;
- $\{R, P, T\}$: Represent orientation matrix, position vector and transformation matrix, respectively.

2.1. Dual-arm system model

The dual-arm manipulator system can be modeled as a closed-chain system with a constraint relationship. The relative positional relationship between the manipulators and the object is as shown in Fig. 2. Where ${}^w l_{(O,T_i)} \in R^{3 \times 1}$ denotes the position vector from the object to the end effectors of the manipulators, and ${}^w l_{(O,T_i)} = [l_x \ l_y \ l_z]^T$, where l_x, l_y and l_z represent the three-dimensional (x, y, z) components of the position vector ${}^w l_{(O,T_i)}$. The relationship between the velocity of the tool frame and object can be expressed as follows:

$$\begin{bmatrix} {}^w v_{T_i} \\ {}^w \omega_{T_i} \end{bmatrix} = \begin{bmatrix} E_3 & O_3 \\ {}^w \hat{l}_{(O,T_i)} & E_3 \end{bmatrix}^T \begin{bmatrix} {}^w v_o \\ {}^w \omega_o \end{bmatrix} \quad (1)$$

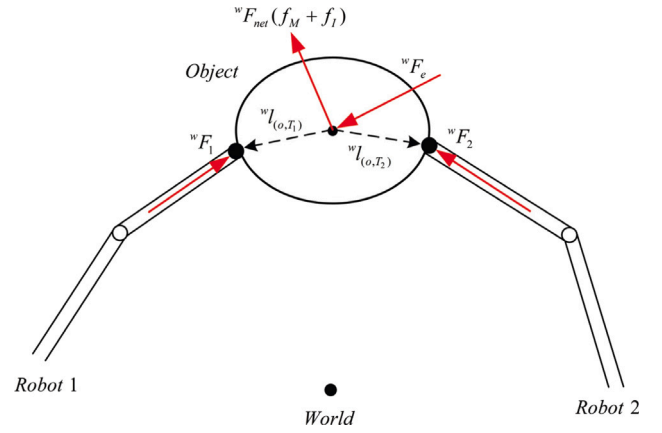


Fig. 2. Relative position and force analysis diagram of a dual-arm manipulators system.

where ${}^w v_{T_i}$ and ${}^w \omega_{T_i}$ are the linear and angular velocity of the tool frame, respectively. ${}^w v_o$ and ${}^w \omega_o$ are the linear and angular velocity of the object, respectively. The \wedge operator transforms a vector to a (3×3) skew symmetric matrix, $\hat{l} = \begin{bmatrix} 0 & -l_z & l_y \\ l_z & 0 & -l_x \\ -l_y & l_x & 0 \end{bmatrix}$. E_3 and O_3 are the identity and zero matrices, respectively. To simplify Eq. 1, the grasp matrix of robot i is defined as $G_i = \begin{bmatrix} E_3 & O_3 \\ {}^w \hat{l}_{(O,T_i)} & E_3 \end{bmatrix}$. Let ${}^w \dot{x}_{T_i} = \begin{bmatrix} {}^w v_{T_i} \\ {}^w \omega_{T_i} \end{bmatrix}$, ${}^w \dot{x}_o = \begin{bmatrix} {}^w v_o \\ {}^w \omega_o \end{bmatrix}$. G_i is the grasp matrix of robot i . Eq. 1 can be rewritten as follows:

$${}^w \dot{x}_{T_i} = G_i^T {}^w \dot{x}_o \quad (2)$$

The velocity constraint relationship between the end effectors of the two manipulators can be expressed as follows:

$$G_1^{-T} \begin{bmatrix} {}^w v_{1} \\ {}^w \omega_{1} \end{bmatrix} = G_2^{-T} \begin{bmatrix} {}^w v_{2} \\ {}^w \omega_{2} \end{bmatrix} \quad (3)$$

$$\begin{bmatrix} G_1^{-T} {}^w R_{R_1} J_{R_1} & -G_2^{-T} {}^w R_{R_2} J_{R_2} \end{bmatrix} \begin{bmatrix} \dot{q}_1 \\ \dot{q}_2 \end{bmatrix} = 0 \quad (4)$$

where J_{R_i} denotes the Jacobian matrix relating the velocities of the robot i base frame, ${}^w \bar{R}_{R_i} = \begin{bmatrix} {}^w R_{R_i} & O_3 \\ O_3 & {}^w R_{R_i} \end{bmatrix}$. ${}^w R_{R_i} \in 3 \times 3$ is the transformation matrices from the robot i base frame to the world frame. Let $G = [G_1 \ G_2]$, ${}^w \dot{x} = \begin{bmatrix} {}^w \dot{x}_1 \\ {}^w \dot{x}_2 \end{bmatrix}$, ${}^w \dot{x}_i = \begin{bmatrix} {}^w v_i \\ {}^w \omega_i \end{bmatrix}$, Eq. 2 can be rewritten as follows:

$${}^w \dot{x} = G^T {}^w \dot{x}_o \quad (5)$$

Differentiating Eq. (5),

$${}^w \ddot{x} = G^T {}^w \ddot{x}_o + \dot{G}^T {}^w \dot{x}_o \quad (6)$$

where $\dot{G}^T {}^w \dot{x}_o = \begin{bmatrix} \dot{G}_1^T {}^w \dot{x}_o \\ \dot{G}_2^T {}^w \dot{x}_o \end{bmatrix}$, and $\dot{G}_i^T {}^w \dot{x}_o = \begin{bmatrix} {}^w \omega_o \times ({}^w \omega_o \times {}^w l_{(O,T_i)}) \\ O \end{bmatrix}$.

2.2. Decomposition of the internal and external forces

The forces exerted on an object during motion include the interaction forces with manipulators and external disturbances imposed by unknown environments. According to Zhang and Khamesee (2017), the object forces can be decomposed into motion-inducing forces and internal forces. A force diagram of the object is shown in Fig. 2.

${}^w F_1$ and ${}^w F_2$ denote the force/moment contributions of the two manipulators at the surface of the object, ${}^w F_{net}$ denotes the net forces on the object, and ${}^w F_e$ denotes an external disturbance. The contact force exerted on the object must be converted into the object centroid.

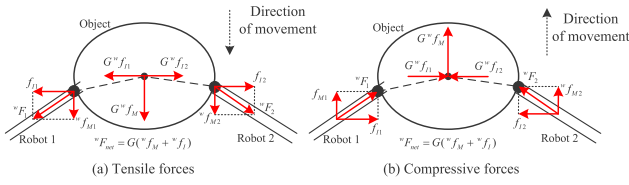


Fig. 3. Diagram illustrating the composition of net forces.

The force and moment relationship between the end effector of the manipulator and the object can be obtained as follows:

$$\begin{cases} {}^w f_o = {}^w f_{T_i} \\ {}^w \tau_o = {}^w \tau_{T_i} + {}^w f_{T_i} \times {}^w l_{(T_i, o)} \end{cases} \quad (7)$$

where ${}^w f_{T_i} \in \mathbb{R}^{3 \times 1}$ and ${}^w \tau_{T_i} \in \mathbb{R}^{3 \times 1}$ are the force and torque components of ${}^w F_i$, respectively. ${}^w f_o \in \mathbb{R}^{3 \times 1}$ and ${}^w \tau_o \in \mathbb{R}^{3 \times 1}$ are the force and torque applied to the object, respectively. ${}^w l_{(T_i, o)} \in \mathbb{R}^{3 \times 1}$ denotes the position vector from the end effectors of the manipulators to the object. For simplicity, Eq. (7) can be rewritten using grasp matrix G , as follows:

$${}^w F_{net} = G^w F \quad (8)$$

where ${}^w F_{net}$ denotes the net forces on the object, ${}^w F = \begin{bmatrix} {}^w F_1 \\ {}^w F_2 \end{bmatrix}$. The grasp matrix is full row rank and $G = \begin{bmatrix} G_1 & G_2 \end{bmatrix}$
 $= \begin{bmatrix} E_3 & O_3 & E_3 & O_3 \\ {}^w \hat{l}_{(o, T_1)} & E_3 & {}^w \hat{l}_{(o, T_2)} & E_3 \end{bmatrix}$. ${}^w F$ can be divided into two parts—that is, motion-inducing (${}^w f_M$) and internal (${}^w f_I$) forces. Hence, ${}^w F = {}^w f_M + {}^w f_I$, and Eq. (8) can be rewritten as follows:

$${}^w F_{net} = G({}^w f_M + {}^w f_I) \quad (9)$$

Fig. 3 illustrates the composition of the net forces, which consist of two parts: motion-inducing ($G^w f_M$) and internal ($G^w f_I$) forces. Notably, not all contact forces contribute to the object motion. Certain contact forces generate tensile or compressive forces on objects, which constitute the internal forces acting upon the object. In practice, only the contact forces can be measured. However, the purpose of intelligent force control algorithms is to control the internal forces. To this end, the internal forces can be calculated. Based on Eq. (9), many researchers have designed a generalized inverse of the grasp matrix to decompose the internal forces (Seraji & Colbaugh, 1997; Zhang & Khamesee, 2017). The pseudo-inverse of the grasp matrix and the weight matrix can be selected as Eq. (10) and (11), respectively:

$$G^\dagger = AG^T(GAG^T)^{-1} \quad (10)$$

$$A = \begin{bmatrix} \Delta & \dots & O_6 \\ \vdots & \ddots & \vdots \\ O_6 & \dots & \Delta \end{bmatrix}, \Delta = \begin{bmatrix} O_3 & I_3 \\ I_3 & O_3 \end{bmatrix} \quad (11)$$

where E_3 and O_3 are the identity and zero matrices, respectively. The motion-inducing and internal forces can be calculated as follows:

$$f_M = (G^\dagger G)^w F \quad (12)$$

$$f_I = (I_{6 \times 2} - G^\dagger G)^w F \quad (13)$$

$${}^w F = G^\dagger F_{net} \quad (14)$$

Remark 1. The calculation of internal forces only requires the position vector from the end effectors of the manipulators to the center of mass of the object and the actual contact forces. By default, the center of mass of the object is assumed to be its geometric center. The actual contact forces can be measured using force sensors. In practice, the position vector can be calculated using the forward kinematics of the manipulators.

Remark 2. The function of the motion-inducing force is to drive the trajectory motion of an object. The internal forces produce only compressive or tensile forces, which do not change the motion dynamics of the object or the contact force. Consequently, it lies within the null space of the grasp matrix.

2.3. Structure of the WNN

Dual-arm manipulators may operate on an unknown object with stiffness and geometric uncertainties. However, traditional constant impedance control cannot compensate for such uncertainties. Therefore, an adaptive WNN can be used for the internal force control of a dual-arm manipulator system, which has been widely used to estimate nonlinear functions owing to its universal approximation capabilities (Hsu, 2013; Zekri, Sadri, & Sheikholeslam, 2008). The WNN includes an input, wavelet, product, and output layer, and its structure is depicted in Fig. 4.

The input layer: $X_i \in \mathbb{R}^{N \times 1}$, $i = 1, 2, \dots, N$. N denotes the number of input elements.

The wavelet layer: The wavelet function can be selected as in Eq. (15), where \hat{c}_{ij} and \hat{b}_{ij} denote the estimated center and width of neural net i , respectively. Φ denotes the output of the wavelet layer, and n denotes the number of layers of the WNN.

$$\begin{cases} \Phi_{ij}(\zeta_{ij}) = (1 - \zeta_{ij}^2) e^{-\frac{1}{2}\zeta_{ij}^2} \\ \zeta_{ij} = \frac{x_j - \hat{c}_{ij}}{\hat{b}_{ij}} \end{cases} \quad (15)$$

$$\Phi = \begin{bmatrix} \Phi_{11} & \Phi_{12} & \dots & \Phi_{1N} \\ \Phi_{21} & \Phi_{22} & \dots & \Phi_{2N} \\ \vdots & \vdots & \dots & \vdots \\ \Phi_{n1} & \Phi_{n2} & \dots & \Phi_{nN} \end{bmatrix} \quad (16)$$

The product layer: $\Psi_i \in \mathbb{R}^{n \times 1}$, $i = 1, 2, \dots, n$

$$\Psi_k = \prod_{i=1}^n \Phi_{ki}(\zeta_{ki}) \quad (17)$$

The output layer: $F(X)$. The output layer function can be expressed as shown in Eq. (18), where $\hat{W}_i \in \mathbb{R}^{k \times 1}$, $i = 1, 2, \dots, k$ denotes the estimated value of the WNN weight matrix, and $F(X)$ denotes the output of the WNN.

$$F(X) = \sum_{k=1}^n \hat{W}_k \Psi_k \quad (18)$$

Remark 3. An adaptive WNN is an online learning algorithm. \hat{c}_{ij} , \hat{b}_{ij} , and \hat{w}_k denote the estimated center, width, and weight of the WNN, respectively. These parameters must be updated and trained using adaptation control laws, the relevant control laws of which are proposed in Section 3. The WNN parameter vector $\hat{\delta}$ can be defined as $\hat{\delta} = [\hat{c}_{11}, \hat{c}_{12}, \dots, \hat{c}_{nN}, \hat{b}_{11}, \hat{b}_{12}, \dots, \hat{b}_{nN}, \hat{W}_1, \hat{W}_2, \dots, \hat{W}_n]^T$.

3. Methods: Dual-arm system coordination strategy

3.1. Problem formulation

Owing to different task requirements, dual-arm manipulators may operate in various unknown workspaces. Disturbances of the external environment—which can cause damage to the dual-arm system—are inevitable. The properties of the operated object—such as its stiffness and geometry—are usually unknown. Additionally, joint bias of the manipulators exists, which can lead to kinematic uncertainty. Consequently, the difficulties of dual-arm manipulator coordination motion can be summarized as follows:

- (1) External disturbances;
- (2) Object stiffness uncertainty; and

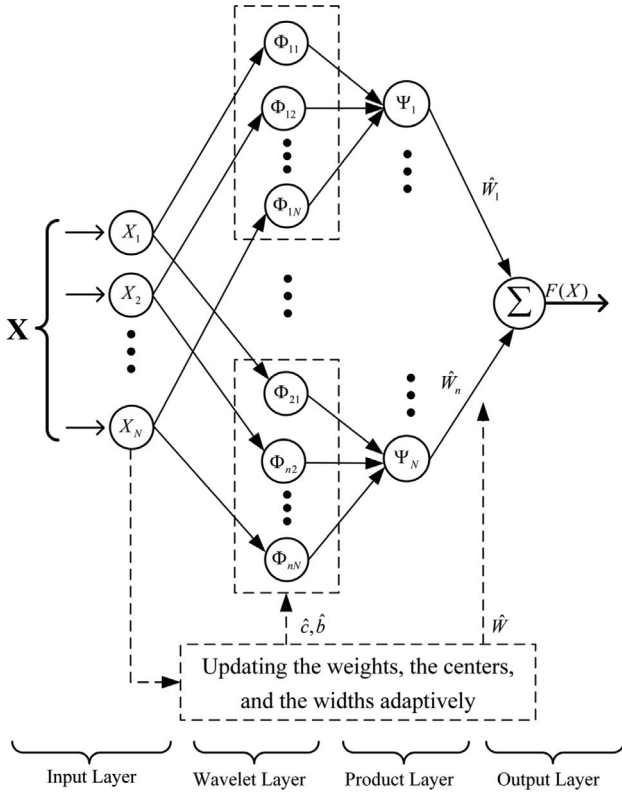


Fig. 4. Structure of the WNN.

(3) Object geometry uncertainty.

External disturbances refer to the forces exerted on the controlled object by the external environment. External disturbances exerted on the manipulator were not considered in this study. These problems require the dual-arm manipulator system to have high degree of adaptability. To address these issues, a two-level adaptive impedance control scheme was proposed, consisting of object-level HIC and manipulator-level NNVSIC. The object-level HIC was used to control the external disturbances and ensure compliant behavior between the object and environment. The manipulator-level NNVSIC was designed to regulate the internal forces. An adaptive WNN was used to compensate for uncertainties.

As demonstrated in Jiao et al. (2022), when an object is operated by a human, the interaction forces could be adjusted by adjusting the arm stiffness, enabling people to increase the arm stiffness to exert more force. Similarly, they could reduce the arm stiffness to reduce the contact force. Motivated by the above study, this study proposed an NNVSIC to regulate the internal forces. It could also maintain the stability of internal force tracking under uncertainties. A block diagram of the NNVSIC is shown in Fig. 5. The algorithm only needs force sensors to measure the end-effector force without an accurate dynamic model. A diagram of the two-level impedances for the dual-arm cooperative system is shown in Fig. 6.

3.2. Object-level hybrid impedance controller

In practice, dual-arm manipulators can operate in a constrained work space (such as welding) or in an unconstrained work space (such as handling). They can be easily disturbed in the process of dual-arm manipulator cooperation. To adapt to two different situations, a HIC comprising two control modes can be used to control external disturbances, that is, the object-level HIC can produce compliant behavior to

avoid damage. The object-level HIC can be expressed as follows:

$$\begin{aligned} \mu_f f_{ed} - f_e &= M_o(\mu_x \ddot{x}_{od} - \ddot{x}_{om}) \\ &+ B_o(\mu_x \dot{x}_{od} - \dot{x}_{om}) + \mu_x K_o(x_{od} - x_{om}) \end{aligned} \quad (19)$$

where f_e denotes the environmental forces exerted on the object including external disturbance forces and contact forces from the environment, and f_{ed} denotes the desired external force, the value of which usually being set to zero for no external disturbance. x_{od} denotes the pre-set desired trajectory and x_{om} denotes the object trajectory after adjustment. M_o , B_o and K_o are the inertia, damping, and stiffness parameters of the object-level HIC, respectively.

Based on the principle of conservation of force, the forces exerted on the object satisfy the relationship $F_a = F_{net} + F_G + f_e$, where F_a denotes the force required to move the object, and F_G denotes the gravity of the object. If the acceleration of the object is small and F_a is negligible, the external disturbance can be calculated as $f_e = -F_{net} - F_G$. Different values of μ_x and μ_f represent different control modes.

$$\begin{cases} \mu_x = 1, \mu_f = 0, & \text{Position control, unconstrained space} \\ \mu_x = 0, \mu_f = 1, & \text{Force control, constraint space} \end{cases} \quad (20)$$

The object-level HIC comprises two control modes—that is, the position control mode and force control mode. When $\mu_x = 1$ and $\mu_f = 0$ (equivalent to setting the desired environment contact force to zero), the object is allowed to follow the desired trajectory. When $\mu_x = 0$ and $\mu_f = 1$ (equivalent to setting the virtual impedance stiffness to zero), the object is allowed to follow the desired contact force. The trajectory after object-level HIC adjustment can be expressed as follows:

$$\begin{aligned} \ddot{x}_{om} &= \mu_x \ddot{x}_{od} + M_o^{-1} [f_e - \mu_f f_{ed} \\ &+ B_o(\mu_x \dot{x}_{od} - \dot{x}_{om}) + \mu_x K_o(x_{od} - x_{om})] \end{aligned} \quad (21)$$

3.3. Manipulator-level neural network-based variable stiffness impedance controller

After the above analysis, the reference trajectory can be adjusted using an object-level HIC, the desired trajectory of the manipulator being calculated using the closed-chain constraint equation. Moreover, the trajectories of the manipulators can be adjusted to regulate the internal forces. Similarly, a manipulator-level constant impedance controller can be expressed as follows:

$$\begin{aligned} f_{Iid} - f_{Ii} &= M_{R_i}(\ddot{x}_{id} - \ddot{x}_{im}) \\ &+ B_{R_i}(\dot{x}_{id} - \dot{x}_{im}) + K_{R_i}(x_{id} - x_{im}) \end{aligned} \quad (22)$$

where f_{Ii} and f_{Iid} denote the actual and desired internal forces of robot i , respectively. The desired internal force is pre-set according to the task requirements. x_{id} and x_{im} denote the desired and adjusted trajectories of robot i , respectively. Typically, the desired trajectory corresponds to the surface of the object, whereas the adjusted trajectory refers to the command trajectory that is transmitted to the manipulator. M_{R_i} , B_{R_i} and K_{R_i} denote the desired positive impedance parameters of robot i .

Assumption 1. The manipulated object is assumed to be rigid. Therefore, the contact force can be expressed as ${}^w F_i = k_{ei} \Delta x_i$, where $k_{ei} \in \mathbb{R}^{6 \times 6}$ denotes the diagonal stiffness matrix of the object, ${}^w F_i \in \mathbb{R}^{6 \times 1}$ is the contact force, $\Delta x_i = x_{id} - x_{im}$, $\Delta x_i \in \mathbb{R}^{6 \times 1}$, and $i = 1, 2$.

Based on Eq. (13), the internal forces can be calculated according to null-space decomposition $f_I = [f_{I1} \quad f_{I2}]^T = (I_{6*2} - G^\dagger G) {}^w F_i$. According to Assumption 1, the internal forces can be expressed as $f_{Ii} = k_{int}(x_{id} - x_{im})$ and $k_{int} = (I_{6*2} - G^\dagger G) k_{ei}$. Subsequently, the manipulator-level constant impedance controller can be expressed as follows:

$$\begin{aligned} f_{Iid} &= M_{R_i}(\ddot{x}_{id} - \ddot{x}_{im}) \\ &+ B_{R_i}(\dot{x}_{id} - \dot{x}_{im}) + K(t)(x_{id} - x_{im}) \end{aligned} \quad (23)$$

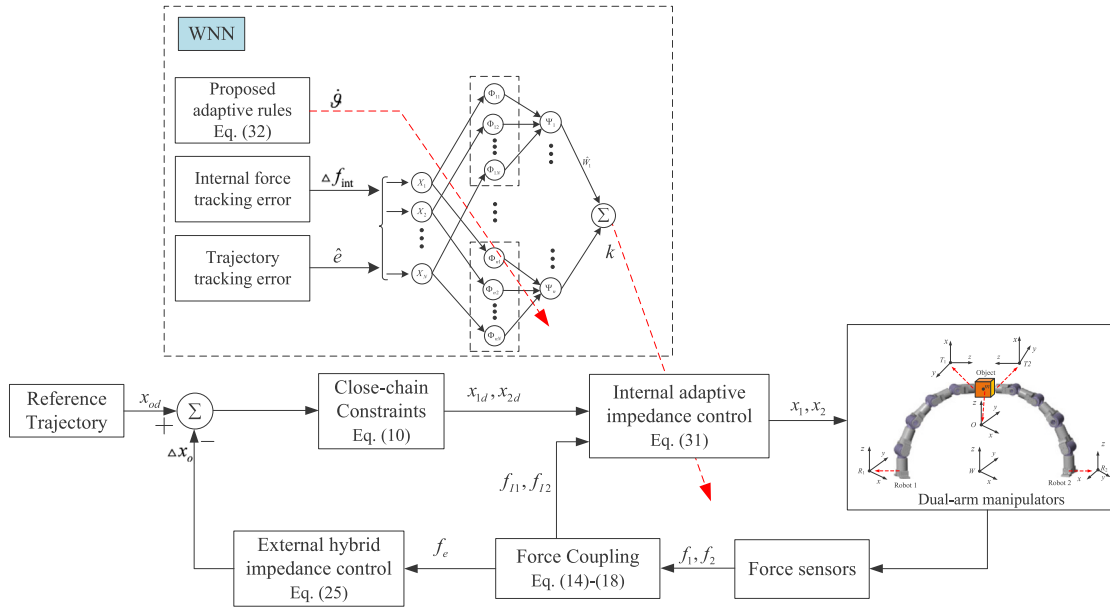


Fig. 5. Block diagram of the proposed two-level adaptive impedance control scheme.

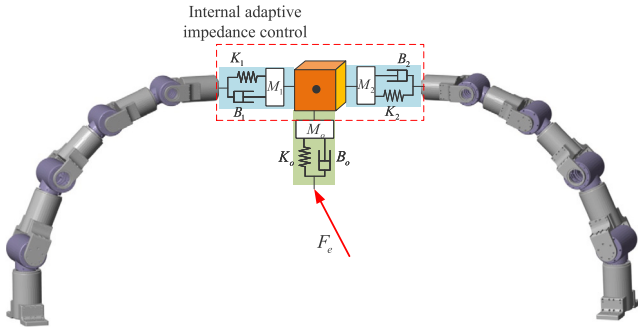


Fig. 6. Diagram of the external and internal impedances for a dual-arm cooperative system.

Remark 4. $K(t) = k_{\text{int}} + K_{R_i}$. The expression of $K(t)$ includes the impedance virtual stiffness and actual stiffness of the object. The uncertainty of object stiffness always exists, $K(t)$ being typically dynamic and unknown in practice.

The internal force tracking error can be expressed as follows:

$$\Delta f_{Ii} = \frac{K_{R_i}}{K_{R_i} + k_{\text{int}}} [k_{\text{int}}(x_{id} - x_{im}) - f_{Iid}] \quad (24)$$

where Δf_{Ii} denotes the internal force-tracking error. The command trajectory of the manipulators must satisfy the following conditions so that Δf_{Ii} converges to zero, as follows:

$$x_{im} = x_{id} - \frac{f_{Iid}}{k_{\text{int}}} \quad (25)$$

However, the desired trajectory cannot be generated for two reasons. First, the desired trajectory of the manipulators is the surface of the object; however, the geometry of the object is uncalibrated and variable, the object geometry uncertainty leading to the desired trajectory deviation of the manipulators. Second, k_{int} is related to the stiffness of the object and grasp matrix, the uncertainty of the object stiffness being the material.

Dual-arm manipulators are usually operated in an uncalibrated environment. Consequently, the error of the desired position of the manipulator can be denoted as δx_{id} , where δ denotes the uncertainty

of the manipulator trajectory caused by the object geometry error. Moreover, $\hat{x}_{id} = x_{id} - \delta x_{id}$, $e_{R_i} = x_{id} - x_{im}$, $\hat{e}_{R_i} = e_{R_i} + \delta x_{id}$, and $\Delta f_{Ii} = f_{Iid} - f_{Ii}$. Thus, Eq. (22) can be expressed as follows:

$$\Delta f_{Ii} = M_{R_i} \ddot{e}_{R_i} + B_{R_i} \dot{e}_{R_i} + K_{R_i} e_{R_i} \quad (26)$$

Based on Eq. (26), setting the stiffness parameter K_{R_i} to zero reduces the internal force-tracking error (Duan et al., 2018; Wahballa et al., 2022). However, owing to the existence of $\delta \dot{x}_{id}$ and $\delta \ddot{x}_{id}$, the internal force-tracking error cannot be completely eliminated. To eliminate the internal force-tracking error, the NNVSIC can be introduced as an online adaptive method to compensate for uncertainties. A block diagram of the proposed NNVSIC is shown in Fig. 7. $K(t)$ can be adjusted by the adaptive WNN. By substituting $K(t)$ into Eq. (26), the manipulator-level NNVSIC can be expressed as follows:

$$\begin{cases} \Delta f_{Ii} = M_{R_i} \ddot{e}_{R_i} + B_{R_i} \dot{e}_{R_i} + K(t) e_{R_i} \\ K(t) = \frac{\hat{F}(X|\hat{\theta})}{\hat{e}} R_i \\ \dot{\hat{\theta}} = \Gamma_{\theta}^T \hat{e}_{R_i} - \beta_1 \hat{\theta} + \beta_2 \Gamma_{\theta}^T \Delta f_{Ii} \\ \Gamma_{\theta} = \frac{\partial \hat{F}(X|\hat{\theta})}{\partial \hat{\theta}} \end{cases} \quad (27)$$

where $\hat{F}(X|\hat{\theta})$ denotes the output of the adaptive WNN, β_1 and β_2 and denote positive gain coefficients. $\Gamma_{\theta} = \left[\frac{\partial \hat{F}(X|\hat{\theta})}{\partial \hat{e}} \quad \frac{\partial \hat{F}(X|\hat{\theta})}{\partial \hat{\theta}} \quad \frac{\partial \hat{F}(X|\hat{\theta})}{\partial \hat{W}} \right]$ is a row vector, and $\dot{\hat{\theta}} = \Gamma_{\theta}^T \hat{e}_{R_i} - \beta_1 \hat{\theta} + \beta_2 \Gamma_{\theta}^T \Delta f_{Ii}$ is an online law that updates the parameters of the WNN. $\Delta f_{Ii} = f_{Iid} - f_{Ii}$ denotes the internal force-tracking error. $\hat{\theta}$ is the WNN parameter vector. Consequently, Eq. (27) can be rewritten as follows:

$$\begin{cases} M_{R_i} \ddot{e}_{R_i} + B_{R_i} \dot{e}_{R_i} = \Delta f_{Ii} - \hat{F}(X|\hat{\theta}) + f_{\delta} \\ \hat{F}(X|\hat{\theta}) = K(t) e_{R_i} \\ f_{\delta} = -(M_{R_i} \delta \ddot{x}_{id} + B_{R_i} \delta \dot{x}_{id}) \\ \dot{\hat{\theta}} = \Gamma_{\theta}^T \hat{e}_{R_i} - \beta_1 \hat{\theta} + \beta_2 \Gamma_{\theta}^T \Delta f_{Ii} \\ \Gamma_{\theta} = \frac{\partial \hat{F}(X|\hat{\theta})}{\partial \hat{\theta}} \end{cases} \quad (28)$$

The control objective is to eliminate the steady-state internal force-tracking error, the principle of this algorithm being to adjust the stiffness coefficient of the impedance controller so that converges to $\hat{F}(X|\hat{\theta})$. If $\hat{F}(X|\hat{\theta}) \rightarrow f_{\delta}$, then Δf_{Ii} converges to zero.

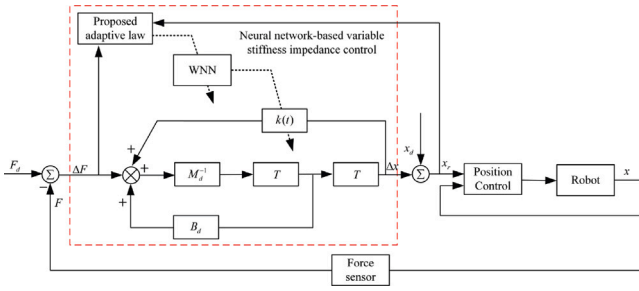


Fig. 7. Block diagram of the NNVSIC.

Assumption 2. The WNN input vector X belongs to the compact set Ω_x . The optimal WNN parameter vector can be assumed to be ϑ^* , which satisfies the following:

$$\vartheta^* = \arg \min \left\{ \sup_{X \in \Omega_x} \left\| F(X|\vartheta^*) - \hat{F}(X|\hat{\vartheta})\hat{\vartheta} \right\| \right\} \quad (29)$$

Assumption 3. The optimal weight vector is bounded by

$$\|\vartheta^*\| \leq \vartheta_{\max} \quad (30)$$

where $\|\cdot\|$ denotes the 2-norm.

Theorem 1. When the optimal parameter value ϑ^* is used to approximate the uncertain term (f_δ), the approximation error is assumed to be ν , and the following equation can be derived:

$$f_\delta = F^*(X|\vartheta^*) + \nu \quad (31)$$

According to Taylor expansion, we can expand $F^*(X|\vartheta^*)$ around $\hat{\vartheta}$, as follows:

$$F^*(X|\vartheta^*) = \hat{F}(X|\hat{\vartheta}) + \tilde{\vartheta}^T \Gamma_\vartheta + h.o(\vartheta^*, \hat{\vartheta}) \quad (32)$$

where $h.o$ denotes the high-order terms of the Taylor expansion, $\tilde{\vartheta} = \vartheta^* - \hat{\vartheta}$. Substituting Eq. (32) into Eq. (31) yields

$$f_\delta = \hat{F}(X|\hat{\vartheta}) + \tilde{\vartheta}^T \Gamma_\vartheta + h.o(\vartheta^*, \hat{\vartheta}) + \nu \quad (33)$$

$$f_\delta = \hat{F}(X|\hat{\vartheta}) + \tilde{\vartheta}^T \Gamma_\vartheta + \sigma \quad (34)$$

Where $\sigma = h.o(\vartheta^*, \hat{\vartheta}) + \nu$.

Assumption 4. σ is assumed to be bounded, satisfying $\|\sigma\| \leq \gamma, \gamma > 0$.

Using Eq. (34), the uncertainty compensation error is $\ell = f_\delta - \hat{F}(X|\hat{\vartheta}) = \tilde{\vartheta}^T \Gamma_\vartheta + \sigma$. Based on the above analysis, the stability of the NNVSIC, as expressed in Eq. (27), can be proven, as discussed in Section 4.

4. Stability analysis

To ensure that the internal force-tracking error can converge to zero, the following Lyapunov function is considered:

$$v = \frac{1}{2} \dot{e}_{R_i}^T \dot{e}_{R_i} + \frac{1}{2} (\tilde{\vartheta}^T \tilde{\vartheta}) \quad (35)$$

By derivation of Eq. (35), we can obtain

$$\dot{v} = \dot{e}_{R_i}^T \ddot{e}_{R_i} + \tilde{\vartheta}^T \dot{\tilde{\vartheta}} \quad (36)$$

According to the impedance equation $\ddot{e}_{R_i} = M_{R_i}^{-1}(-B_{R_i} \dot{e}_{R_i} + \Delta f_{li} + \ell)$, yielding

$$\begin{aligned} \dot{v} &= \dot{e}_{R_i}^T M_{R_i}^{-1}(-B_{R_i} \dot{e}_{R_i} + \Delta f_{li} + \ell) + \tilde{\vartheta}^T \dot{\tilde{\vartheta}} \\ &= -\dot{e}_{R_i}^T M_{R_i}^{-1} B_{R_i} \dot{e}_{R_i} + M_{R_i}^{-1} \dot{e}_{R_i}^T \Delta f_{li} \\ &\quad + M_{R_i}^{-1} \dot{e}_{R_i}^T \ell + \tilde{\vartheta}^T \dot{\tilde{\vartheta}} \end{aligned} \quad (37)$$

According to Theorem 1, $\ell = f_\delta - \hat{F}(X|\hat{\vartheta}) = \tilde{\vartheta}^T \Gamma_\vartheta + \sigma$

$$\begin{aligned} \dot{v} &= -\dot{e}_{R_i}^T M_{R_i}^{-1} B_{R_i} \dot{e}_{R_i} + M_{R_i}^{-1} \dot{e}_{R_i}^T \Delta f_{li} \\ &\quad + M_{R_i}^{-1} \dot{e}_{R_i}^T (\tilde{\vartheta}^T \Gamma_\vartheta + \sigma) + \tilde{\vartheta}^T \dot{\tilde{\vartheta}} \end{aligned} \quad (38)$$

Where $\tilde{\vartheta} = \vartheta^* - \hat{\vartheta}$, $\vartheta^* = \text{constant}$, $\dot{\tilde{\vartheta}} = -\dot{\hat{\vartheta}}$, yielding

$$\begin{aligned} \dot{v} &= -\dot{e}_{R_i}^T M_{R_i}^{-1} B_{R_i} \dot{e}_{R_i} + M_{R_i}^{-1} \dot{e}_{R_i}^T \Delta f_{li} \\ &\quad + M_{R_i}^{-1} \dot{e}_{R_i}^T (\tilde{\vartheta}^T \Gamma_\vartheta + \sigma) - \tilde{\vartheta}^T \dot{\hat{\vartheta}} \\ &= -\dot{e}_{R_i}^T M_{R_i}^{-1} B_{R_i} \dot{e}_{R_i} + M_{R_i}^{-1} \dot{e}_{R_i}^T \Delta f_{li} \\ &\quad + M_{R_i}^{-1} \dot{e}_{R_i}^T \sigma + \tilde{\vartheta}^T (M_{R_i}^{-1} \dot{e}_{R_i}^T \Gamma_\vartheta - \dot{\hat{\vartheta}}) \end{aligned} \quad (39)$$

According to the NNVSIC Eq. (27), the parameter update law of the WNN is $\dot{\hat{\vartheta}} = M_{R_i}^{-1} \Gamma_\vartheta^T \dot{e}_{R_i} - \beta_1 \hat{\vartheta} + \beta_2 \Gamma_\vartheta^T \Delta f_{li}$. Substituting this into Eq. (39), we obtain

$$\begin{aligned} \dot{v} &= -\dot{e}_{R_i}^T M_{R_i}^{-1} B_{R_i} \dot{e}_{R_i} + M_{R_i}^{-1} \dot{e}_{R_i}^T \Delta f_{li} + M_{R_i}^{-1} \dot{e}_{R_i}^T \sigma \\ &\quad + \tilde{\vartheta}^T (M_{R_i}^{-1} \dot{e}_{R_i}^T \Gamma_\vartheta - M_{R_i}^{-1} \Gamma_\vartheta^T \dot{e}_{R_i} + \beta_1 \hat{\vartheta} - \beta_2 \Gamma_\vartheta^T \Delta f_{li}) \end{aligned} \quad (40)$$

where $\dot{e}_{R_i} = \dot{e}_{R_i} + \delta \dot{x}_{id}$.

$$\begin{aligned} \dot{v} &= -\dot{e}_{R_i}^T M_{R_i}^{-1} B_{R_i} \dot{e}_{R_i} + M_{R_i}^{-1} \dot{e}_{R_i}^T \Delta f_{li} + M_{R_i}^{-1} \dot{e}_{R_i}^T \sigma \\ &\quad + \tilde{\vartheta}^T (M_{R_i}^{-1} \dot{e}_{R_i}^T \Gamma_\vartheta - M_{R_i}^{-1} \Gamma_\vartheta^T (\dot{e}_{R_i} + \delta \dot{x}_{id})) \\ &\quad + \tilde{\vartheta}^T (\beta_1 \hat{\vartheta} - \beta_2 \Gamma_\vartheta^T \Delta f_{li}) \end{aligned} \quad (41)$$

$$\begin{aligned} &= -\dot{e}_{R_i}^T M_{R_i}^{-1} B_{R_i} \dot{e}_{R_i} + M_{R_i}^{-1} \dot{e}_{R_i}^T \Delta f_{li} + M_{R_i}^{-1} \dot{e}_{R_i}^T \sigma \\ &\quad + \tilde{\vartheta}^T (-M_{R_i}^{-1} \Gamma_\vartheta^T \delta \dot{x}_{id} + \beta_1 \hat{\vartheta} - \beta_2 \Gamma_\vartheta^T \Delta f_{li}) \end{aligned} \quad (42)$$

$$\begin{aligned} \dot{v} &= -\dot{e}_{R_i}^T M_{R_i}^{-1} B_{R_i} \dot{e}_{R_i} + M_{R_i}^{-1} \dot{e}_{R_i}^T \Delta f_{li} + M_{R_i}^{-1} \dot{e}_{R_i}^T \sigma \\ &\quad - M_{R_i}^{-1} (\tilde{\vartheta}^T \Gamma_\vartheta)^T \delta \dot{x}_{id} + \beta_1 \tilde{\vartheta}^T \hat{\vartheta} - \beta_2 (\tilde{\vartheta}^T \Gamma_\vartheta)^T \Delta f_{li} \\ &= -\dot{e}_{R_i}^T M_{R_i}^{-1} B_{R_i} \dot{e}_{R_i} + M_{R_i}^{-1} \dot{e}_{R_i}^T \Delta f_{li} + M_{R_i}^{-1} \dot{e}_{R_i}^T \sigma \\ &\quad - M_{R_i}^{-1} (\ell - \sigma)^T \delta \dot{x}_{id} + \beta_1 \tilde{\vartheta}^T \hat{\vartheta} - \beta_2 (\tilde{\vartheta}^T \Gamma_\vartheta)^T \Delta f_{li} \end{aligned} \quad (42)$$

As $\hat{\vartheta} = \vartheta^* - \tilde{\vartheta}$, Eq. (42) can be rewritten as follows:

$$\begin{aligned} \dot{v} &= -\dot{e}_{R_i}^T M_{R_i}^{-1} B_{R_i} \dot{e}_{R_i} + M_{R_i}^{-1} \dot{e}_{R_i}^T \Delta f_{li} + M_{R_i}^{-1} \dot{e}_{R_i}^T \sigma \\ &\quad - M_{R_i}^{-1} (\ell - \sigma)^T \delta \dot{x}_{id} + \beta_1 \tilde{\vartheta}^T (\vartheta^* - \tilde{\vartheta}) \\ &\quad - \beta_2 (\tilde{\vartheta}^T \Gamma_\vartheta)^T \Delta f_{li} \end{aligned} \quad (43)$$

Based on Eq. (28), then

$$\begin{aligned} \Delta f_{li} &= M_{R_i} \ddot{e}_{R_i} + B_{R_i} \dot{e}_{R_i} - (\hat{F}(X|\hat{\vartheta}) - f_\delta) \\ &= p - (\tilde{\vartheta}^T \Gamma_\vartheta + \sigma) \end{aligned} \quad (44)$$

where $p = M_{R_i} \ddot{e}_{R_i} + B_{R_i} \dot{e}_{R_i}$.

Substituting Eq. (44) into Eq. (43) yields

$$\begin{aligned} \dot{v} &= -\dot{e}_{R_i}^T M_{R_i}^{-1} B_{R_i} \dot{e}_{R_i} + M_{R_i}^{-1} \dot{e}_{R_i}^T \Delta f_{li} + M_{R_i}^{-1} \dot{e}_{R_i}^T \sigma \\ &\quad - M_{R_i}^{-1} (\ell - \sigma)^T \delta \dot{x}_{id} + \beta_1 \tilde{\vartheta}^T \vartheta^* - \beta_1 \tilde{\vartheta}^T \tilde{\vartheta} \\ &\quad - \beta_2 (\tilde{\vartheta}^T \Gamma_\vartheta)^T (p - \tilde{\vartheta}^T \Gamma_\vartheta - \sigma) \\ &= -\dot{e}_{R_i}^T M_{R_i}^{-1} B_{R_i} \dot{e}_{R_i} + M_{R_i}^{-1} \dot{e}_{R_i}^T \Delta f_{li} + M_{R_i}^{-1} \dot{e}_{R_i}^T \sigma \\ &\quad - M_{R_i}^{-1} (\ell - \sigma)^T \delta \dot{x}_{id} + \beta_1 \tilde{\vartheta}^T \vartheta^* - \beta_1 \tilde{\vartheta}^T \tilde{\vartheta} \\ &\quad + \beta_2 (\tilde{\vartheta}^T \Gamma_\vartheta)^T \tilde{\vartheta}^T \Gamma_\vartheta - \beta_2 (\tilde{\vartheta}^T \Gamma_\vartheta)^T (p - \sigma) \end{aligned} \quad (45)$$

Using the fact $2ab \leq a^2 + b^2$, the following inequality can be obtained:

$$\begin{aligned} \frac{\beta_1}{2} 2\tilde{\vartheta}^T \vartheta^* &\leq \frac{\beta_1}{2} \tilde{\vartheta}^T \tilde{\vartheta} + \frac{\beta_1}{2} \vartheta^{*T} \vartheta^* \\ &\leq \frac{\beta_1}{2} \tilde{\vartheta}^T \tilde{\vartheta} + \frac{\beta_1}{2} \vartheta_{\max}^T \vartheta_{\max} \end{aligned} \quad (46)$$

$$\begin{aligned} -\beta_2 (\tilde{\vartheta}^T \Gamma_\vartheta)^T (p - \sigma) &= -\beta_2 (\tilde{\vartheta}^T \Gamma_\vartheta)^T p + \beta_2 (\tilde{\vartheta}^T \Gamma_\vartheta)^T \sigma \\ &\leq \beta_2 ((\tilde{\vartheta}^T \Gamma_\vartheta)^T)^2 + \frac{\beta_2}{2} p^2 + \frac{\beta_2}{2} \sigma^2 \end{aligned} \quad (47)$$

$$M_{R_i}^{-1} \dot{e}_{R_i}^T \sigma \leq \frac{M_{R_i}^{-1}}{2} (\dot{e}_{R_i}^T)^2 + \frac{M_{R_i}^{-1}}{2} \sigma^2 \quad (48)$$

$$-M_{R_i}^{-1} (\ell - \sigma)^T \delta \dot{x}_{id} \leq \frac{M_{R_i}^{-1}}{2} ((\tilde{\vartheta}^T \Gamma_\vartheta)^T)^2 + \frac{M_{R_i}^{-1}}{2} (\delta \dot{x}_{id})^2 \quad (49)$$

By substituting Eqs. (46)–(49) into Eq. (45), we obtain

$$\begin{aligned}
\dot{v} \leq & -\dot{e}_{R_i}^T M_{R_i}^{-1} B_{R_i} \dot{e}_{R_i} + M_{R_i}^{-1} \dot{e}_{R_i}^T \Delta f_{li} + M_{R_i}^{-1} \dot{e}_{R_i}^T \sigma \\
& - M_{R_i}^{-1} (\ell - \sigma)^T \delta \dot{x}_{id} + \frac{\beta_1}{2} \vartheta_{\max}^T \vartheta_{\max} - \frac{\beta_1}{2} \bar{\vartheta}^T \bar{\vartheta} \\
& + \beta_2 (\bar{\vartheta}^T \Gamma_{\vartheta})^T \bar{\vartheta}^T \Gamma_{\vartheta} - \beta_2 (\bar{\vartheta}^T \Gamma_{\vartheta})^T (p - \sigma) \\
\leq & -\dot{e}_{R_i}^T M_{R_i}^{-1} B_{R_i} \dot{e}_{R_i} + M_{R_i}^{-1} \dot{e}_{R_i}^T \Delta f_{li} + M_{R_i}^{-1} \dot{e}_{R_i}^T \sigma \\
& - M_{R_i}^{-1} (\ell - \sigma)^T \delta \dot{x}_{id} + \frac{\beta_1}{2} \vartheta_{\max}^T \vartheta_{\max} - \frac{\beta_1}{2} \bar{\vartheta}^T \bar{\vartheta} \\
& + \beta_2 (\bar{\vartheta}^T \Gamma_{\vartheta})^T \bar{\vartheta}^T \Gamma_{\vartheta} + \beta_2 (\bar{\vartheta}^T \Gamma_{\vartheta})^T)^2 + \frac{\beta_2}{2} p^2 + \frac{\beta_2}{2} \sigma^2 \\
\leq & -\dot{e}_{R_i}^T M_{R_i}^{-1} (B_{R_i} - \frac{1}{2}) \dot{e}_{R_i} - \frac{\beta_1}{2} \bar{\vartheta}^T \bar{\vartheta} + M_{R_i}^{-1} \dot{e}_{R_i}^T \Delta f_{li} \\
& + \frac{M_{R_i}^{-1}}{2} (\delta \dot{x}_{id})^2 + \frac{\beta_1}{2} \vartheta_{\max}^T \vartheta_{\max} + \frac{\beta_2}{2} p^2 + \frac{1}{2} (\beta_2 + M_{R_i}^{-1}) \sigma^2 \\
& + (2\beta_2 + \frac{M_{R_i}^{-1}}{2}) (\bar{\vartheta}^T \Gamma_{\vartheta})^T)^2
\end{aligned} \tag{50}$$

Defining $\beta_2^* = (2\beta_2 + \frac{M_{R_i}^{-1}}{2}) \Gamma_{\vartheta}^T \Gamma_{\vartheta}$ yields

$$\begin{aligned}
\dot{v} \leq & -\dot{e}_{R_i}^T M_{R_i}^{-1} (B_{R_i} - \frac{1}{2}) \dot{e}_{R_i} - (\frac{\beta_1}{2} - \beta_2^*) \bar{\vartheta}^T \bar{\vartheta} \\
& + M_{R_i}^{-1} \dot{e}_{R_i}^T \Delta f_{li} + \frac{M_{R_i}^{-1}}{2} (\delta \dot{x}_{id})^2 + \frac{\beta_1}{2} \vartheta_{\max}^T \vartheta_{\max} \\
& + \frac{\beta_2}{2} p^2 + \frac{1}{2} (\beta_2 + M_{R_i}^{-1}) \sigma^2
\end{aligned} \tag{51}$$

Defining $\alpha_1 = M_{R_i}^{-1} (B_{R_i} - \frac{1}{2})$, $\alpha_2 = \frac{\beta_1}{2} - \beta_2^*$ yields

$$\begin{aligned}
\dot{v} \leq & -\alpha_1 \dot{e}_{R_i}^T \dot{e}_{R_i} - \alpha_2 \bar{\vartheta}^T \bar{\vartheta} + M_{R_i}^{-1} \dot{e}_{R_i}^T \Delta f_{li} + \frac{M_{R_i}^{-1}}{2} (\delta \dot{x}_{id})^2 \\
& + \frac{\beta_1}{2} \vartheta_{\max}^T \vartheta_{\max} + \frac{\beta_2}{2} p^2 + \frac{1}{2} (\beta_2 + M_{R_i}^{-1}) \sigma^2 \\
\leq & -\alpha_1 \dot{e}_{R_i}^T \dot{e}_{R_i} - \alpha_2 \bar{\vartheta}^T \bar{\vartheta} + M_{R_i}^{-1} \dot{e}_{R_i}^T \Delta f_{li} + \frac{M_{R_i}^{-1}}{2} (\delta \dot{x}_{id})^2 \\
& + \frac{\beta_1}{2} \vartheta_{\max}^T \vartheta_{\max} + \frac{\beta_2}{2} p^2 + \frac{1}{2} (\beta_2 + M_{R_i}^{-1}) \sigma^2
\end{aligned} \tag{52}$$

We can define $\Xi = M_{R_i}^{-1} \dot{e}_{R_i}^T \Delta f_{li} + \frac{M_{R_i}^{-1}}{2} (\delta \dot{x}_{id})^2 + \frac{\beta_1}{2} \vartheta_{\max}^T \vartheta_{\max} + \frac{\beta_2}{2} p^2 + \frac{1}{2} (\beta_2 + M_{R_i}^{-1}) \sigma^2$, where $M_{R_i}^{-1}$ has a small value, thus,

$$\dot{v} \leq -\alpha_1 \dot{e}_{R_i}^T \dot{e}_{R_i} - \alpha_2 \bar{\vartheta}^T \bar{\vartheta} + \Xi \tag{53}$$

Finally, we can define $0 < \rho \leq \min[\alpha_1, \alpha_2]$. Based on Eq. (53), we can obtain the following:

$$\dot{v} \leq -2\rho v + \Xi \tag{54}$$

Here, Eq. (54) can be multiplied by $e^{2\rho t}$, to yield:

$$\dot{v} e^{2\rho t} \leq -2\rho v e^{2\rho t} + \Xi e^{2\rho t} \tag{55}$$

$$\dot{v} e^{2\rho t} + 2\rho v e^{2\rho t} \leq \Xi e^{2\rho t} \tag{56}$$

$$\frac{d}{dt} (v e^{2\rho t}) \leq \Xi e^{2\rho t} \tag{57}$$

Integrating Eq. (57) yields,

$$v \leq v(0) e^{-2\rho t} - \frac{\Xi}{2\rho} e^{-2\rho t} + \frac{\Xi}{2\rho} \tag{58}$$

If $\lim_{t \rightarrow +\infty} \frac{\Xi}{2\rho} e^{-2\rho t} > 0$, then Eq. (58) can be rewritten as follows:

$$v \leq v(0) e^{-2\rho t} + \frac{\Xi}{2\rho} \tag{59}$$

The error vector can be defined as shown in Eq. (60) and the compact set can be defined as shown in Eq. (61):

$$P = \left[\begin{array}{c} \dot{e} \\ \|\bar{\vartheta}\| \end{array} \right]^T \tag{60}$$

$$\Omega = \left\{ \|P\| \leq \sqrt{2(V(0)e^{-2\rho t} + \frac{\Xi}{2\rho})} \right\} \tag{61}$$

Table 1
Experimental object properties.

Material	Mass	Surface	Stiffness	Geometry
Balloon	0.02 kg	Non-Flat	520 N/m	uncertain
Sponge	0.04 kg	Non-Flat	1000 N/m	0.19*0.12*0.06 m
Cardboard box	0.3 kg	Flat	4500 N/m	0.21*0.1*0.15 m
Plastic box	0.5 kg	Flat	6100 N/m	0.2*0.2*0.2 m

From the above discussion, if $v < \frac{\Xi}{2\rho}$, $-2\rho v + \Xi > 0$, and $\dot{v} \leq 0$, the error vector (P) converges asymptotically to the compact set Ω .

5. Results and discussion

5.1. Experimental hardware and software platform

To demonstrate the performance of the proposed NNVSIC, a series of experiments were conducted with two self-developed 9-DOF redundant manipulators. The experimental platform is shown in Fig. 8.

The software system includes a servo driver, robot kinematic control, and force distribution and decoupling applications, as well as a two-level impedance controller, the adaptive WNN control law, and the EtherCAT communication protocol. The hardware system comprises two self-developed 9-DOF redundant manipulators, two ATI six-dimensional force sensors, a computer, CX2020 Beckhoff controllers, motor drives, and the manipulated objects. As shown in Fig. 8, the distance between the two redundant manipulators is approximately 1.2 m. The force sensors are installed at the end effectors of the manipulators. The sampling rate of the ATI six-dimensional force sensors is 200 Hz, the force sensors providing feedback on the collected contact forces to the controller and the controller calculating the actual internal and external forces of the object. The controllers are used for sensor information collection, kinematics calculation, algorithm implementation, and module communication. The servo drives are used to control the joint motor movement of the manipulators. All modules communicate via the EtherCAT protocol, the communication period being 5 ms. The aim of the experiment is to verify the effectiveness and superiority of the two-level adaptive impedance control scheme under various uncertainties—such as disturbance, stiffness, and geometry uncertainties. To prove that the NNVSIC are sufficient to describe all types of variable stiffness objects, four different experimental materials, including soft (balloon and sponge) and hard (cardboard box and plastic box) objects, were chosen to conduct the experiments. The object properties are listed in Table 1. Different experimental objects are shown in Fig. 9.

After a series of measurements using a force sensor, the stiffnesses of the balloon and sponge are approximately 520 and 1100 N/m, respectively. The boxes are harder with stiffnesses of 6100 and 4500 N/m, respectively. Additionally, the geometry of the balloon is uncertain and varies during cooperative motion. Owing to the uncalibrated geometry of the object and uncalibrated relative positions of the two manipulators, position estimation errors always exist, all factors that bring about difficulties in the collaborative movement. The experiments were divided into two parts—that is, manipulation of the hard objects and manipulation of the soft objects. To verify the adaptability of the algorithm, all parameters of the WNN—including the initial conditions, centers, widths, and weights of the WNN—were the same in the different experiments. This meant that the optimal stiffness parameters could only be adjusted by the WNN adaptive control law. The input of the NN was the position deviation (\dot{e}_{R_i}) and internal tracking error (Δf_{li}), and the output of the NN was the stiffness of the NNVSIC. The number of wavelet layers was eight. Additionally, three internal force control algorithms were chosen for comparison with the proposed NNVSIC, the three controllers being the constant impedance controller (Method 1: CIC), the variable damping impedance controller (Method 2: VDIC) (Jinjun et al., 2019), and the variable stiffness impedance

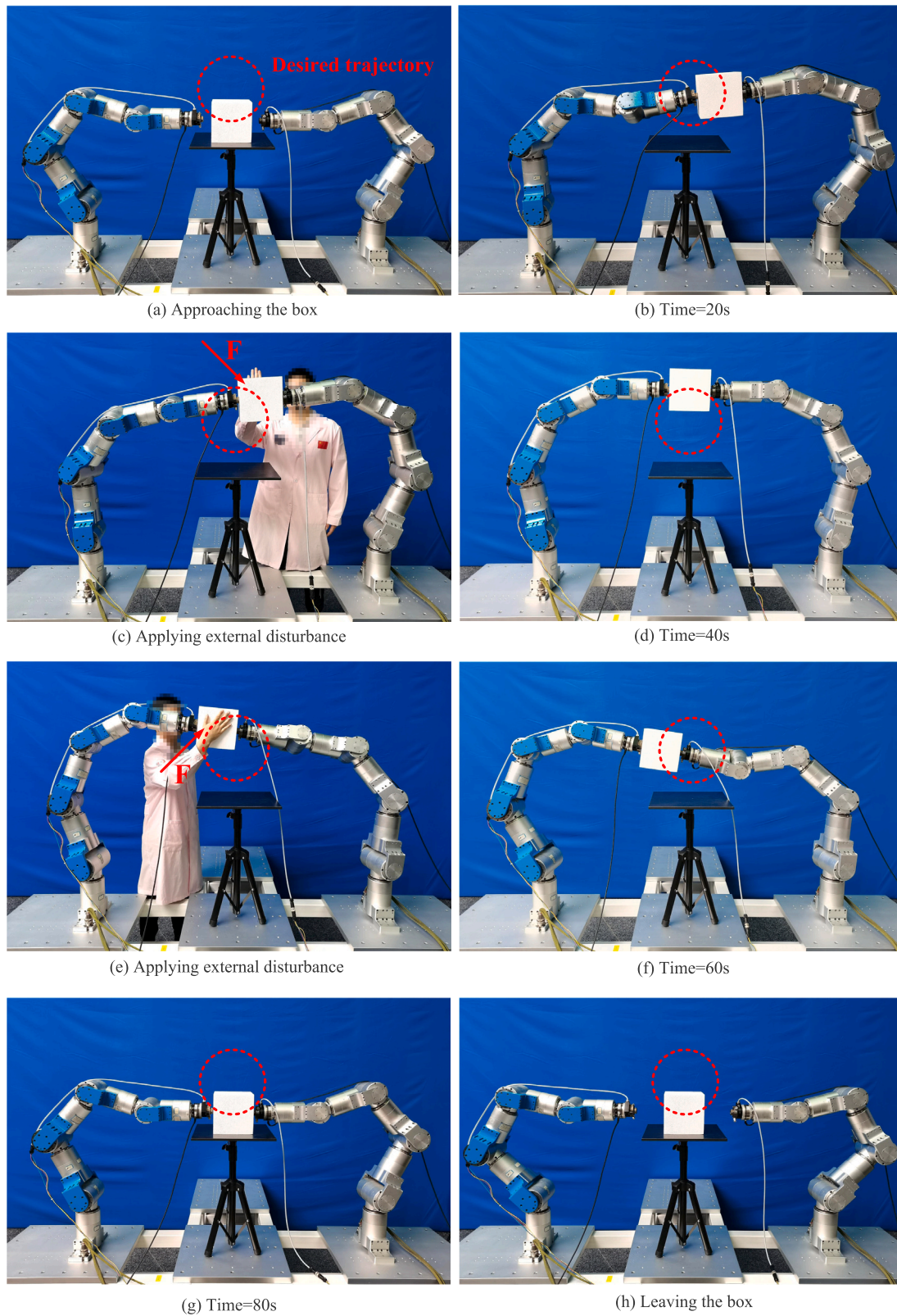


Fig. 10. Collaborative movement process when manipulating a box.

in Fig. 14. The manipulators are not initially in touch with the object because the surface of the object is unknown. Thus, the internal forces are initially zero. Because the box is hard, the manipulators only need

to move a short distance to make contact with the box, meaning the required internal force can be tracked quickly, the setting time being 3.52 s. An internal force-tracking error is inevitable because of the

Table 2
Experimental parameters.

Controller		Parameter value
Method 1		$M_{R_i} = 200, B_{R_i} = 3000, K_{R_i} = 0$
Method 2		$M_{R_i} = 200, B_{R_i} = 3500, K_{R_i} = 0, \sigma = 0.08$
Method 3		$M_{R_i} = 200, B_{R_i} = 3300, K_{R_i} = 0, \lambda = 0.05$
Two-level adaptive impedance control scheme	Object-level HIC	$M_{R_i} = 300, B_{R_i} = 500, K_{R_i} = 700, \mu_x = 1, \mu_f = 0$
	Manipulator-level NNVSIC	$M_{R_i} = 200, B_{R_i} = 4600, K_{R_i} = K(t), \beta_1 = 0.25, \beta_2 = 1.2, n = 8, \dot{W} = 10$

Table 3
Internal force-tracking performance when manipulating hard objects.

Material	Trajectory	Method	Setting time (s)	Steady-state error (N)	Overshoot (%)	IAE	RMSE	
Plastic box	Circle	Method 1	9.96	51	146.91	584.98	12.08	
		Method 2	4.05	4.3	78.19	162.47	3.96	
		Method 3	6.6	4.5	83.3	172.04	3.86	
		NNVSIC	3.8	4.5	47.11	161.48	3.45	
Plastic box	Rectangle	Method 1	1.86	34	89.29	449.8	10.54	
		Method 2	4.19	6.3	19.81	118.9	3.27	
		Method 3	2.69	7.3	42.43	222.68	5.09	
		NNVSIC	1.44	4.2	14.57	97.59	2.88	
Cardboard box	Circle	Method 1	3.22	21	74.43	312.88	5.84	
		Method 2	3.13	3.2	31.76	111.82	2.85	
		Method 3	2.2	4.1	45.66	117.83	2.82	
		NNVSIC	2.02	3.3	21.01	106.40	2.62	
	Cardboard box	Rectangle	Method 1	1.6	30.7	105.51	812.5	15.77
			Method 2	1.23	5.7	27.57	100.04	3.12
			Method 3	1.8	5.5	31.8	113.38	3.23
			NNVSIC	1.78	3.2	21.8	87.11	2.85

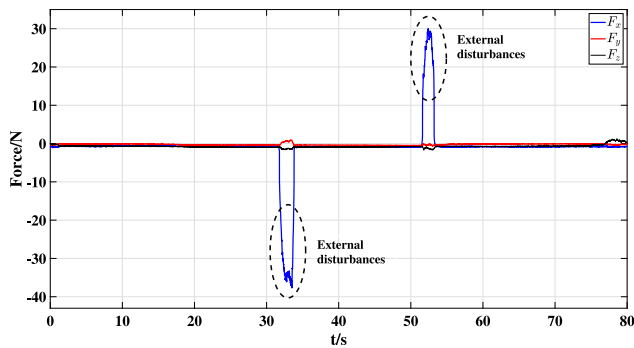


Fig. 11. External disturbances exerted on the box.

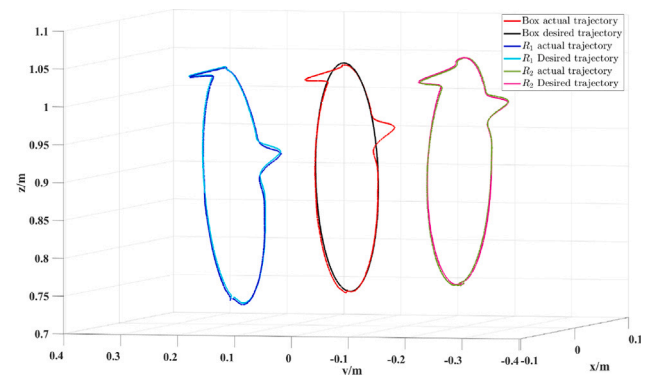


Fig. 13. Dual-arm manipulators cooperative motion trajectory.

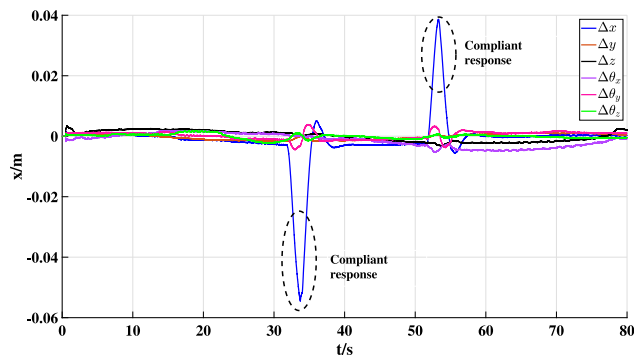


Fig. 12. Box trajectory deviation under external disturbances.

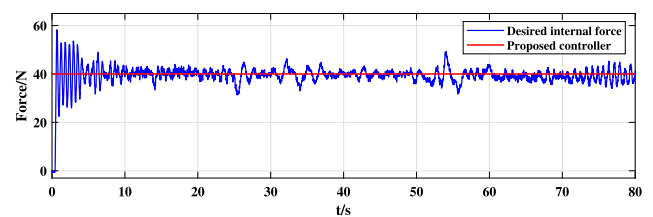


Fig. 14. Internal force tracking under external disturbances during box manipulation.

existence of trajectory tracking deviations and external disturbances. Because the stiffness of the box is large and there are position tracking

errors, a small position deviation can lead to a large force-tracking error. The steady-state force-tracking error is approximately 4.5 N. Because of the external force, the internal force changes abruptly at 35 and 53 s, the peak internal force being 48.56 N. Despite this, the internal force is always tracked within a range. Although the stiffness and geometry of the box are unknown in advance, the internal force can also be tracked based on the proposed NNVSIC.

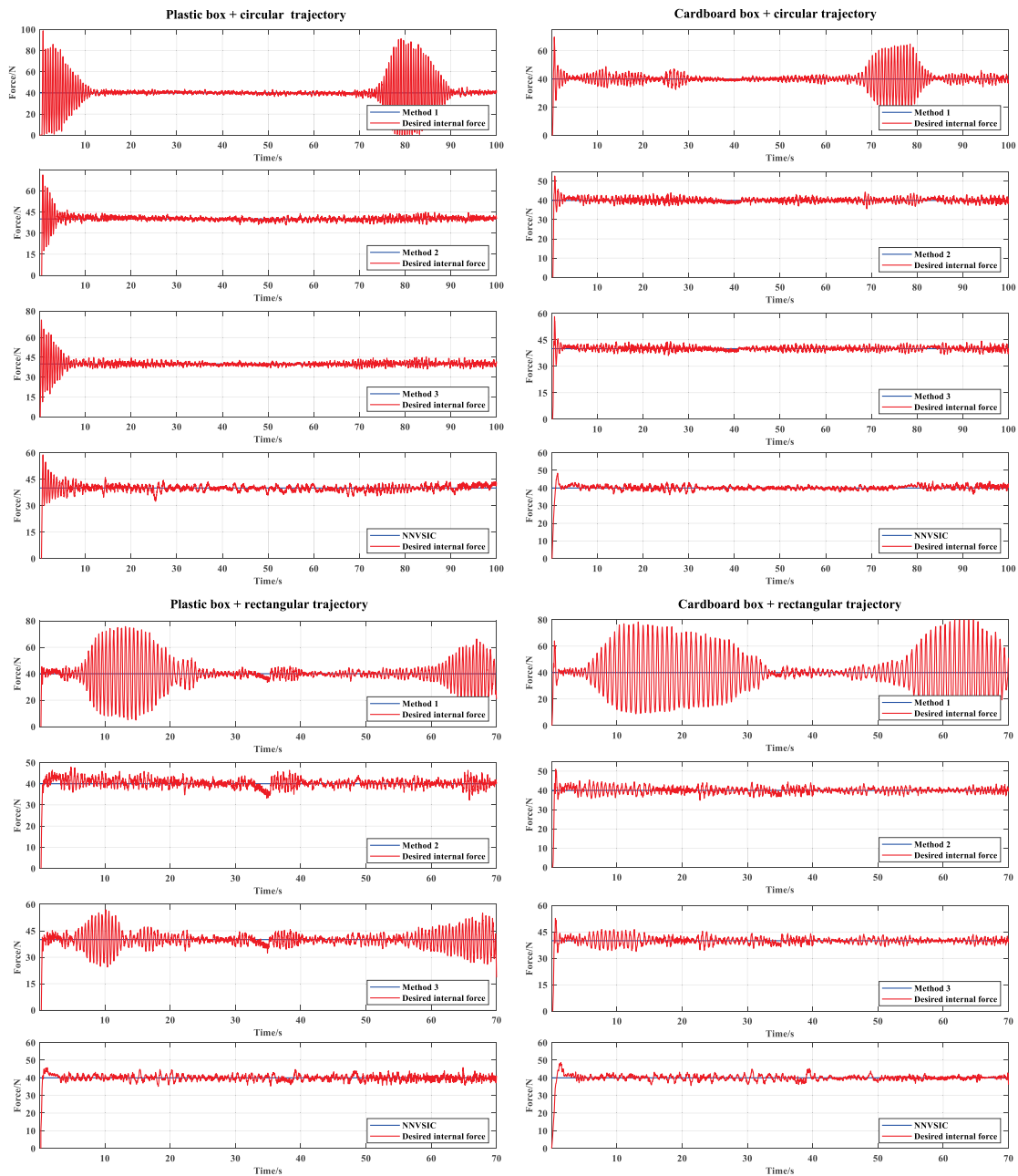


Fig. 15. Internal force tracking results for various controllers when manipulating hard objects.

5.2.2. Internal force-tracking performance comparison

In this subsection, four different algorithms are compared to verify their internal force-tracking performance. Method 1 represents the traditional CIC, Method 2 represents the VDIC proposed in Jinjun et al. (2019), and Method 3 represents the VSIC based on force feedback proposed in Jiao et al. (2022). In this experiment, the plastic and cardboard boxes were manipulated along circular and rectangular trajectories, respectively, the internal force-tracking response curves of the four algorithms being as shown in Fig. 15. The traditional algorithm exhibits a large overshoot and slow convergence speed, the internal force oscillating considerably initially. Owing to uncertain factors—such as the stiffness and geometric uncertainties—the internal force does not remain stable all the time as it oscillates again at 70 s, the chattering phenomenon demonstrating the instability of traditional CIC. The VDIC proposed in the literature was also examined. Its algorithm can maintain the stability of the internal force, although its overshoot is 30.9 N higher than that of the proposed algorithm (18.2 N). The

proposed NNVSIC outperforms the other algorithms in terms of forces control under different trajectories and for different objects.

Five performance metrics—that is, the response time, steady-state error, overshoot, IAE, and RMSE—were selected to evaluate the algorithms, the relevant experimental results being presented in Table 3. The proposed algorithm achieves perfect internal force-tracking performance when manipulating two types of boxes, moving along both the circular and rectangular trajectories. However, the internal force oscillates when manipulating a large box using the VDIC and VSIC. This is because the stiffness and trajectory deviation of the controlled object change and the adaptive adjustment abilities of the VDIC and VSIC are inadequate. The response time, steady-state error, overshoot, IAE, and RMSE of the proposed controller are less than those of the other algorithms.

The internal force-tracking performance described by a radar map is illustrated in Fig. 16. Five performance metrics are depicted on the five-dimensional coordinates of the radar map—the smaller the

Table 4
Internal force-tracking performance when manipulating soft objects.

Material	Trajectory	Method	Setting time (s)	Steady-state error (N)	Overshoot (%)	IAE	RMSE
Sponge	Circle	Method 1	35.5	2.1	4.75	148.6	3.81
		Method 2	34.4	0.53	30.72	110.1	2.92
		Method 3	39	0.7	18.11	106	2.86
		NNVSIC	13.9	0.51	18	62.07	2.58
	Rectangle	Method 1	38	2.2	8.25	148.3	3.88
		Method 2	35	0.33	29.33	103.5	2.86
		Method 3	35	0.9	23.61	98.63	2.73
		NNVSIC	13.8	0.39	21.11	65.83	2.72
Balloon	Circle	Method 1	37.1	1.1	5.9	253.15	5.77
		Method 2	14.2	0.6	57.54	314.6	5.82
		Method 3	17.01	0.5	37.44	289.18	5.13
		NNVSIC	12.35	0.3	19.76	145.3	4.39
	Rectangle	Method 1	38.2	1.1	4.56	246.5	6.25
		Method 2	14.9	0.5	60.84	326.12	6.72
		Method 3	15.03	0.9	44.88	341.47	6.55
		NNVSIC	13.5	0.2	18.95	175	5.26

area enclosed by the three performance indicators, the better the internal force-tracking performance. As is evident from Fig. 16, the proposed controller encloses a smaller area than the other two algorithms, compensating for uncertainties and adapting to unknown objects. Compared with the CIC, VDIC, and VSIC, the control performance of the NNVSIC is superior.

5.3. Manipulating soft objects

In practice, the manipulator usually needs to carry objects of different stiffnesses. In this subsection, experiments manipulating soft objects using dual-arm manipulators are described. A balloon has a lower stiffness and more irregular surface when compared to a box. To verify the robustness and adaptability of the algorithm, all experimental parameters and initial conditions were consistent with the previous box-manipulation experiments.

5.3.1. Compliance test

Similarly, external disturbances can be exerted on balloons by humans in the process of cooperative movement, the collaborative movement process being as shown in Fig. 17. Moreover, the external disturbance exerted on the object when manipulating a balloon is as shown in Fig. 18. The trajectory deviation and cooperative motion trajectory of the dual-arm manipulator system are shown in Figs. 19 and 20, respectively. When a force is applied to an object, the manipulators move away from the external disturbance, the compliance of the HIC being independent of the manipulated object. This is related to the external disturbance and impedance parameters. Owing to external disturbances, the trajectory tracking error is adjusted, the object being compliant with the environment.

The desired internal force was set as 15 N on the Y-axis. The internal force-tracking results when manipulating a balloon under an external disturbance are shown in Fig. 21. The internal force-tracking error under external disturbances is 4 N, the range of internal force variation being 26.7%. Compared with manipulating boxes, the internal force changes are more evident for two reasons. One reason is that balloons are softer and more likely to deform when external disturbances are applied, the external disturbance being likely to cause a change in internal forces. Another reason is that the stiffness of the balloon is lower, and the manipulator needs to move further to maintain the internal force, the balloon taking longer to respond than the boxes. Consequently, the results shown in Fig. 21 can be considered to be reasonable. After a period of adjustment, the internal force-tracking error gradually converges to zero. Even though the stiffness and geometry of the object change, the control scheme can still realize internal force tracking.

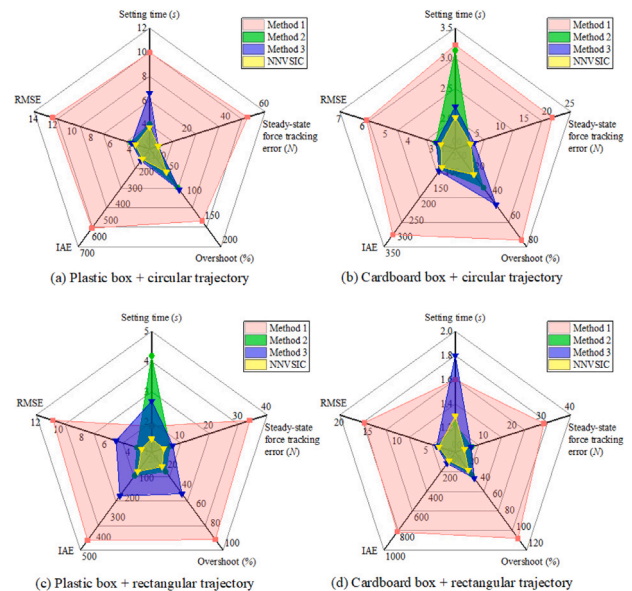


Fig. 16. Comparison of the internal force-tracking performance when manipulating hard objects.

5.3.2. Internal force-tracking performance comparison

Similarly, the other three algorithms were compared with the NNVSIC. Two materials with different stiffnesses and geometries and two experimental trajectories (i.e., circle and rectangle) were selected to verify the performance of the proposed NNVSIC when manipulating soft objects. Internal force tracking could not be realized using the traditional CIC, VDIC, or VSIC because the stiffness and geometry of the object changed. The original control parameters did not meet the stability requirements of the control system, and the adaptive control law designed by the algorithm could not adapt to the changes in object stiffness. The overshoot, setting time, and steady-state error of the proposed algorithm were 23.3%, 29.8 s, and 0.3 N, respectively. Although the VDIC could compensate for these uncertainties, its overshoot and steady-state error were worse than those of the proposed NNVSIC. Lower IAE and RMSE values also prove the superiority of the NNVSIC. Additionally, an inappropriate control factor was also a reason for poor tracking performance, both the CIC and VDIC relying on appropriate impedance parameters. The manipulated object was usually uncalibrated, making the preselection of the impedance parameters difficult.

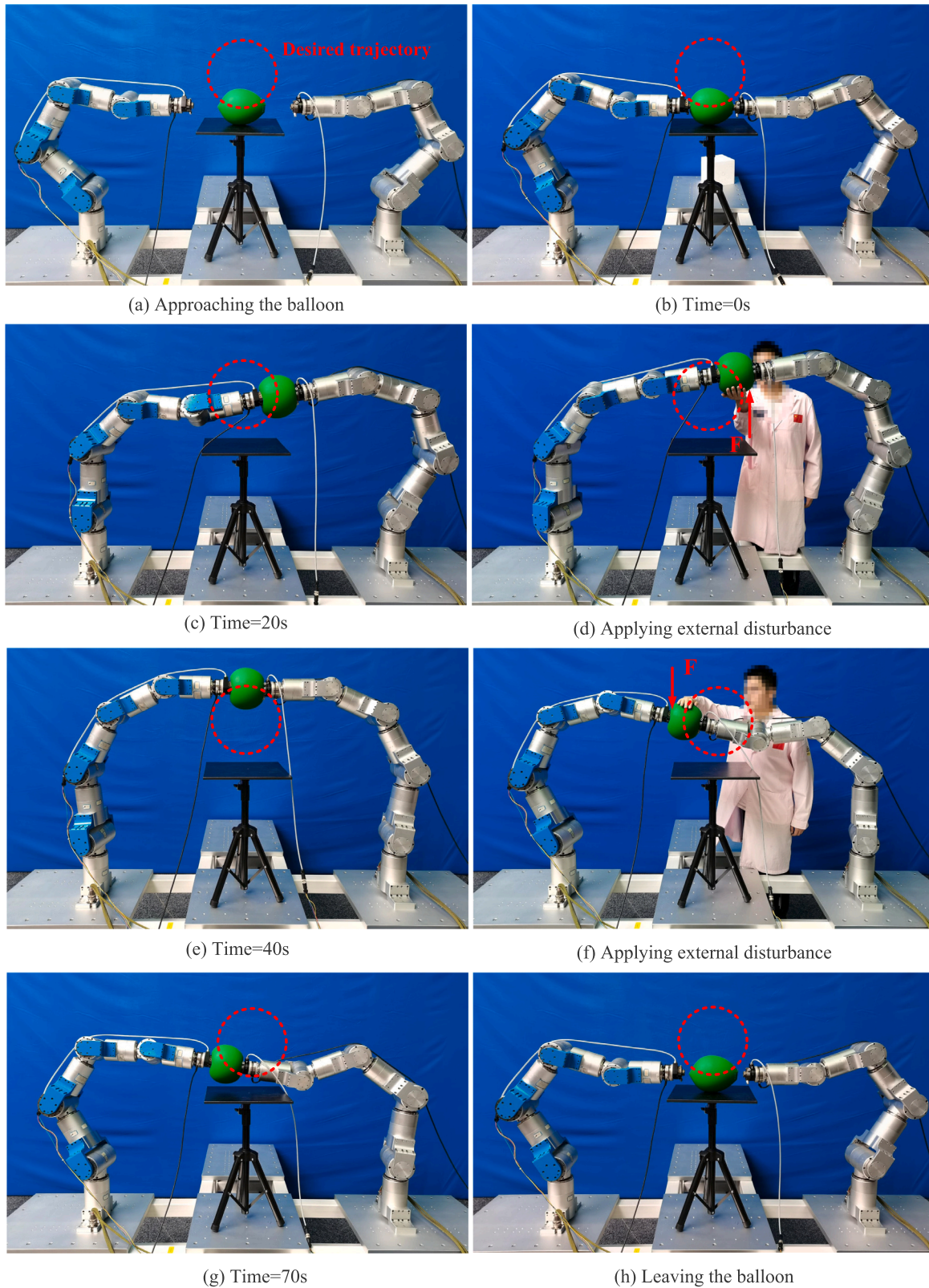


Fig. 17. Collaborative movement process when manipulating a balloon.

By contrast, the adaptive WNN exhibited better adaptability. The proposed NNVSIC achieves excellent control performance for both the circular and rectangular trajectories. Internal force tracking was still realized with the same impedance parameters using the proposed controller. Although soft objects have less stiffness than hard objects and

a longer distance is required to achieve the desired internal force, the NNVSIC responded faster than the other algorithms. The steady-state error of the soft object was smaller than that of the hard object because their stiffness was lower, and the force caused by the same trajectory deviation was smaller, depending on the properties of the object.

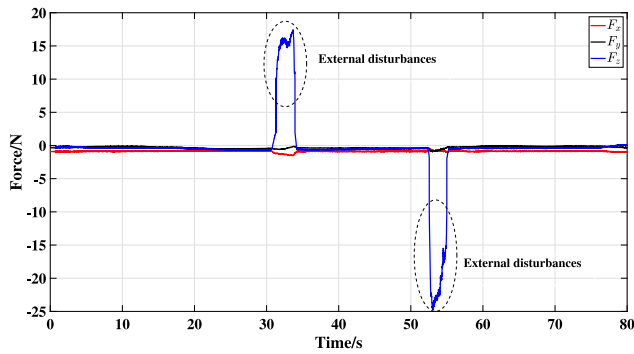


Fig. 18. External disturbances exerted on the balloon.

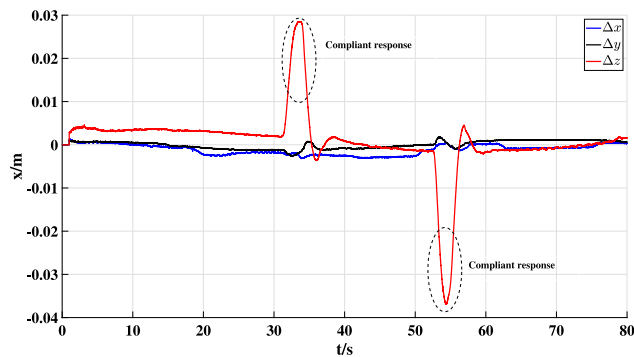


Fig. 19. Object trajectory deviation under external disturbances.

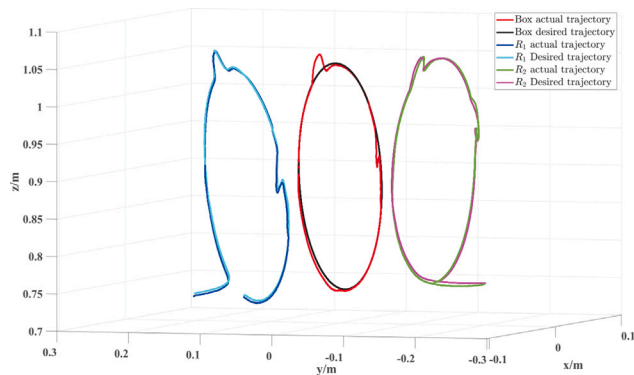


Fig. 20. Dual-arm cooperative motion trajectories.

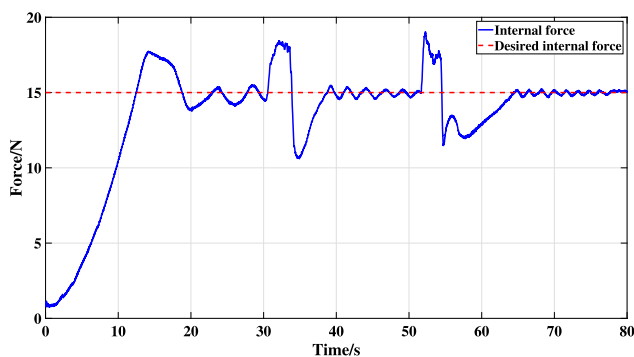


Fig. 21. Internal force tracking under external disturbances when manipulating a balloon.

However, compared with other algorithms, the proposed NNVSIC still exhibited a smaller steady-state error owing to its excellent controller performance.

The internal force tracking results are shown in Table 4 and Fig. 22. The internal force-tracking performance described by the radar map is shown in Fig. 23, the smaller the area in the radar map, the better the performance. Regardless of the soft material and motion trajectory used, it is evident from Fig. 23 that the NNVSIC has the smallest area. In summary, the external HIC can establish compliance between the object and environment, and the NNVSIC can effectively compensate for stiffness and geometric uncertainties to achieve stable internal force tracking.

5.4. Discussion

In the experiments, the hard and soft objects were tested under two different trajectories based on four algorithms. Under different experimental conditions, the force-tracking results exhibit different convergence properties. Regardless of the material and motion trajectory used, it is evident that the proposed NNVSIC exhibits the smallest area, as shown in Figs. 16 and 23. The CIC, VDIC and VSIC, exhibit limitations when controlling different objects. For example, the CIC oscillates when controlling a hard object and converges more slowly. The VDIC and VSIC exhibit larger overshoots and integral absolute errors. The reason for the unsatisfactory tracking performance exhibited by these algorithms is that the range of stiffness change of the object is too large; consequently, the different algorithms cannot properly adjust the internal force. That is, the algorithms lack adaptive abilities. The relative position error of the manipulators, geometric estimation error of the object, and position deviation due to manipulator jitter also cause internal force tracking instability. In contrast, the proposed NNVSIC exhibits an excellent control performance.

The adaptive variable stiffness control law designed in this study simulated the adjusting stiffness of the human arm. When the force deviation was large, it indicated that the actual internal force had not reached the desired value, making it necessary to provide a large stiffness to reduce the force deviation. When the force deviation was small, it was not necessary to provide a large stiffness to adjust the internal force. In practice, the stiffness of the manipulator should be as soft as possible to maintain the internal force as the force deviation approaches zero.

Fig. 24 shows the stiffness adjustment process. At the time of initialization, the NNVSIC initial stiffness parameter of 13,500 for handling both soft and hard objects is large. This parameter is determined by the initialization of the NN parameters. At this point, the actual internal force differs considerably from the desired internal force. The stiffness parameters are maintained at a relatively high level for the first 10 s, as the internal force has not yet converged to the desired value, and a stiffness value is needed to ensure the convergence speed of the internal forces is as fast as possible and the overshoot as small as possible. Moreover, when manipulating hard objects, the stiffness of the NNVSIC decreases faster than when manipulating soft objects. This is influenced by the convergence rate of the two materials. Hard objects reach the target internal force value faster. Accordingly, the stiffness decreases faster.

From 10–30 s, the internal force gradually converges to the desired internal force, the force deviation is small, and a stiffness value is no longer required to adjust the internal force. Consequently, the stiffness parameter gradually converges to zero. Additionally, the blue curve in Fig. 24 shows the internal force instability when an external disturbance is exerted on the object. From 19–30 s, two external disturbances are applied to the object, the NNVSIC providing a large stiffness value to resist the external disturbance and maintain the internal force stability as much as possible. As the disturbance disappears, the internal force is retraced, and the stiffness returns to zero, the arm being as soft as possible. The NN converts the instability factors in the actual system into variable stiffness. Under system instability, the stiffness value can play a regulating role to promote the stability of the system.

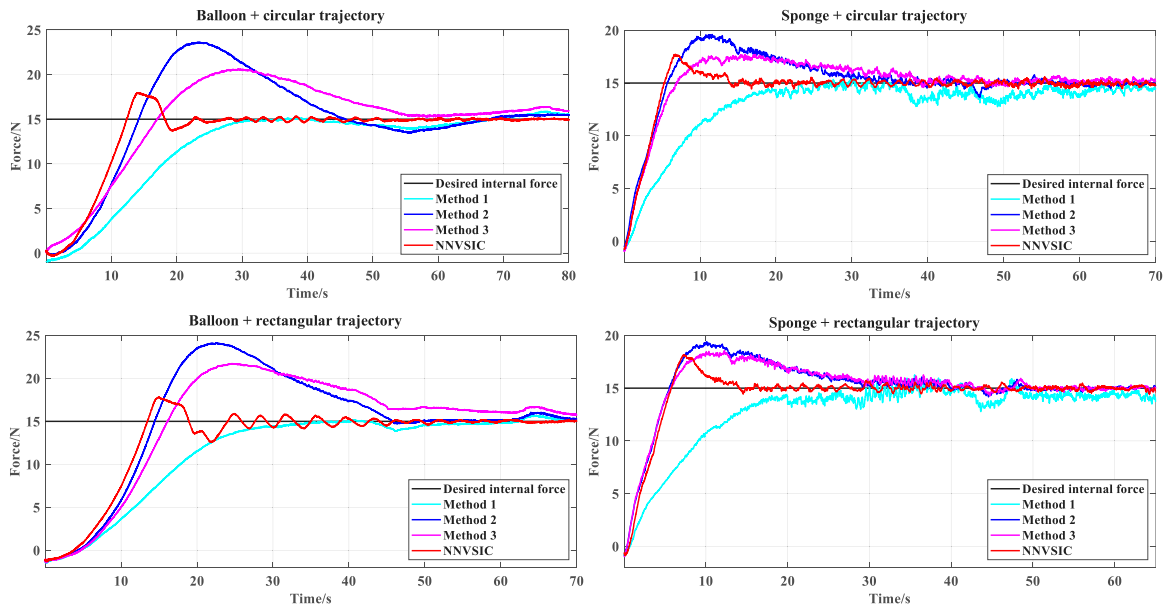


Fig. 22. Internal force-tracking results for various controllers when manipulating soft objects.

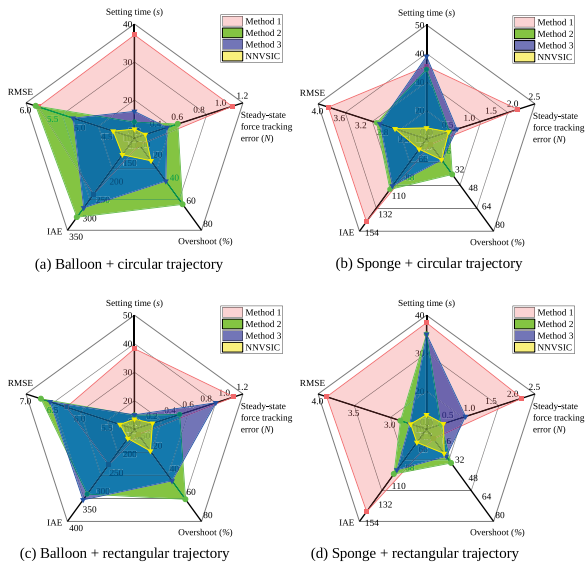


Fig. 23. Internal force-tracking performance comparison when manipulating soft objects.

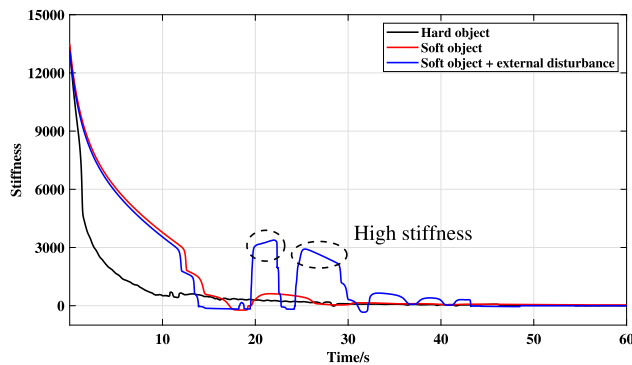


Fig. 24. Stiffness curves of the proposed NNVSIC.

6. Conclusion

In this study, a two-level adaptive impedance control scheme was proposed for dual-arm manipulator systems that manipulate uncertain objects, uncertain factors such as external disturbance, stiffness, and geometric uncertainties being considered. The external HIC adjusted the desired trajectory in response to external forces, thereby making the controlled object compliant with the environment, the internal forces being controlled using an NNVSIC. Moreover, the stability of the controller was proven using the Lyapunov stability theory. The performance of the controller was verified experimentally on hard and soft objects. Based on the experimental results, the proposed controller exhibited perfect internal force-tracking performance regardless of whether it manipulated hard or soft objects, and the same experimental parameters could adapt to objects of different stiffnesses and geometries. Compared with other algorithms, the proposed method exhibited a better performance in terms of response speed, overshoot, steady-state error, IAE, and RMSE, proving the effectiveness and superiority of the proposed control scheme.

To further improve the relevant research outcomes of this study and extend the results to practical multi-robot cooperation application, several suggestions for future work should be considered:

- (1) Disturbance observers should be designed to observe contact forces and avoid the use of force sensors.
- (2) Only external disturbances applied to the object were considered, and no external disturbances were applied to the manipulators. In the future, a null-space impedance control loop could be added to enhance the null-space compliance.

Funding

This research was supported by the National Natural Science Foundation of China (Grant Nos. 62173047, 62235018).

CRediT authorship contribution statement

Yufei Zhou: Conceptualization, Methodology, Software, Data curation, Writing – original draft. **Zhongcan Li:** Methodology, Software, Validation, Writing – review & editing. **Yanhui Li:** Investigation, Resources, Visualization, Supervision. **Mingchao Zhu:** Project administration, Funding acquisition.

Declaration of competing interest

The authors declare that they have no known competing financial interests or personal relationships that could have appeared to influence the work reported in this paper.

Data statement

The data used in this study is available upon request from the corresponding author. Due to privacy and ethical considerations, we are unable to publicly share the data directly. However, we are committed to promoting transparency and reproducibility in research. Therefore, we encourage interested researchers to contact the corresponding author to request access to the data used in this study.

Acknowledgments

We are grateful to the National Natural Science Foundation of China for providing financial support for this research. This funding has enabled us to conduct the necessary experiments, collect data, and analyze the results. We would like to express our heartfelt gratitude to Chinese academy of Science (CAS) Key Laboratory of On-orbit Manufacturing for their unwavering support and invaluable contributions to this research.

References

- Aghili, F. (2010). Robust impedance control of manipulators carrying a heavy payload. *Journal of Dynamic Systems, Measurement, and Control*, 132(5).
- Bonitz, R. C., & Hsia, T. C. (1996). Internal force-based impedance control for cooperating manipulators. *IEEE Transactions on Robotics and Automation*, 12(1), 78–89.
- Calanca, A., Muradore, R., & Fiorini, P. (2015). A review of algorithms for compliant control of stiff and fixed-compliance robots. *IEEE/ASME Transactions on Mechatronics*, 21(2), 613–624.
- Cao, H., He, Y., Chen, X., et al. (2020). Smooth adaptive hybrid impedance control for robotic contact force tracking in dynamic environments. *Industrial Robot: the International Journal of Robotics Research and Application*, 47(2), 231–242.
- Chen, Z., Guo, Q., Li, T., et al. (2022). Gait prediction and variable admittance control for lower limb exoskeleton with measurement delay and extended-state-observer. *IEEE Transactions on Neural Networks and Learning Systems*.
- Chien, S. H., Wang, J. H., & Cheng, M. Y. (2021). Robotic assistance for physical human–robot interaction using a fuzzy RBF hand impedance compensator and a neural network based human motion intention estimator. *IEEE Access*, 9, Article 126048-126057.
- Chung, J. H., Yi, B. J., & Kim, W. K. (2005). Analysis of internal loading at multiple robotic systems. *Journal of Mechanical Science and Technology*, 19, 1554–1567.
- Dong, J., Xu, J., Zhou, Q., et al. (2020). Physical human–robot interaction force control method based on adaptive variable impedance. *Journal of the Franklin Institute*, 357(12), 7864–7878.
- Duan, J., Gan, Y., Chen, M., et al. (2018). Adaptive variable impedance control for dynamic contact force tracking in uncertain environment. *Robotics and Autonomous Systems*, 102, 54–65.
- Erhart, S., & Hirche, S. (2015). Internal force analysis and load distribution for cooperative multi-robot manipulation. *IEEE Transactions on Robotics*, 31(5), 1238–1243.
- Ferraguti, F., Landi, C., Talignani, S., Sabattini, L., et al. (2019). A variable admittance control strategy for stable physical human–robot interaction. *International Journal of Robotics Research*, 38(6), 747–765.
- Gierlak, P., & Szuster, M. (2017). Adaptive position/force control for robot manipulator in contact with a flexible environment. *Robotics and Autonomous Systems*, 95, 80–101.
- Gueaieb, W., Karray, F., & Al-Sharhan, S. (2007). A robust hybrid intelligent position/force control scheme for cooperative manipulators. *IEEE/ASME Transactions on Mechatronics*, 12(2), 109–125.
- Guo, Q., Zhang, Y., Celler, B. G., & Su, S. W. (2019). Neural adaptive backstepping control of a robotic manipulator with prescribed performance constraint. *IEEE Transactions on Neural Networks and Learning Systems*, 30(12), 3572–3583.
- Hamedani, M. H., Sadeghian, H., Zekri, M., et al. (2021). Intelligent impedance control using wavelet neural network for dynamic contact force tracking in unknown varying environments. *Control Engineering Practice*, 113, Article 104840.
- He, W., & Dong, Y. (2017). Adaptive fuzzy neural network control for a constrained robot using impedance learning. *IEEE Transactions on Neural Networks and Learning Systems*, 29(4), 1174–1186.
- Hsu, C.-F. (2013). Adaptive neural complementary sliding-mode control via functional-linked wavelet neural network. *Engineering Applications of Artificial Intelligence*, 26(4), 1221–1229.
- Hu, H., & Cao, J. (2022). Adaptive variable impedance control of dual-arm robots for slabstone installation. *ISA Transactions*, 128, 397–408.
- Jiang, Y., Wang, Y., Miao, Z., et al. (2020). Composite-learning-based adaptive neural control for dual-arm robots with relative motion. *IEEE Transactions on Neural Networks and Learning Systems*.
- Jiao, C., Yu, L., Su, X., et al. (2022). Adaptive hybrid impedance control for dual-arm cooperative manipulation with object uncertainties. *Automatica*, 140, Article 110232.
- Jinjun, D., Yahui, G., Ming, C., et al. (2019). Symmetrical adaptive variable admittance control for position/force tracking of dual-arm cooperative manipulators with unknown trajectory deviations. *Robotics and Computer-Integrated Manufacturing*, 57, 357–369.
- Jung, S., & Hsia, T. C. (2000a). Robust neural force control scheme under uncertainties in robot dynamics and unknown environment. *IEEE Transactions on Industrial Electronics*, 47(2), 403–412.
- Jung, S., & Hsia, T. C. (2000b). Robust neural force control scheme under uncertainties in robot dynamics and unknown environment. *IEEE Transactions on Industrial Electronics*, 47(2), 403–412.
- Jung, S., Hsia, T. C., & Bonitz, R. G. (2004). Force tracking impedance control of robot manipulators under unknown environment. *IEEE Transactions on Control Systems Technology*, 12(3), 474–483.
- Kang, T., Yi, J.-B., Song, D., & Yi, S.-J. (2021). High-speed autonomous robotic assembly using in-hand manipulation and re-grasping. *Applied Sciences*, 11(1), 37.
- Kim, R., Balakirsky, S., Ahlin, K., et al. (2021). Enhancing payload capacity with dual-arm manipulation and adaptable mechanical intelligence. *Journal of Mechanisms and Robotics*, 13(2).
- Kim, T., Yoo, S., Seo, T., Kim, H. S., & Kim, J. (2020). Design and force-tracking impedance control of 2-DOF wall-cleaning manipulator via disturbance observer. *IEEE/ASME Transactions on Mechatronics*.
- Lee, J., Chang, P. H., & Jamisola, R. S. (2013). Relative impedance control for dual-arm robots performing asymmetric bimanual tasks. *IEEE Transactions on Industrial Electronics*, 61(7), 3786–3796.
- Lee, C. H., & Wang, W. C. (2016). Robust adaptive position and force controller design of robot manipulator using fuzzy neural networks. *Nonlinear Dynamics*, 85, 343–354.
- Liu, T., Lei, Y., Han, L., et al. (2016). Coordinated resolved motion control of dual-arm manipulators with closed chain. *International Journal of Advanced Robotic Systems*, 13(3), 80.
- Mohajerpour, R., Rezaei, M., Talebi, A., et al. (2012). A robust adaptive hybrid force/position control scheme of two planar manipulators handling an unknown object interacting with an environment. *Proceedings of the Institution of Mechanical Engineers, Part I: Journal of Systems and Control Engineering*, 226(4), 509–522.
- Nguyen, T. V., Thai, N. H., Phan, T. A., et al. (2019). Adaptive neural network based backstepping sliding mode control approach for dual-arm robots. *Journal of Control Automation and Electrical Systems*.
- Ochoa, H., & Cortesao, R. (2021). Impedance control architecture for robotic-assisted mold polishing based on human demonstration. *IEEE Transactions on Industrial Electronics*.
- Panwar, V., Kumar, N., Sukavanam, N., et al. (2012). Adaptive neural controller for cooperative multiple robot manipulator system manipulating a single rigid object. *Applied Soft Computing*, 12(1), 216–227.
- Rani, M., Kumar, N., & Singh, H. P. (2019). Motion/force control scheme for electrically driven cooperative multiple mobile manipulators. *Control Engineering Practice*, 88, 52–64.
- Sadeghian, H., Ficuciello, F., Villani, L., et al. (2012). Global impedance control of dual-arm manipulation for safe interaction. *IFAC Proceedings Volumes*, 45(22), 767–772.
- Sadeghian, H., Villani, L., Keshmiri, M., et al. (2013). Task-space control of robot manipulators with null-space compliance. *IEEE Transactions on Robotics*, 30(2), 493–506.
- Seraji, H., & Colbaugh, R. (1997). Force tracking in impedance control. *International Journal of Robotics Research*, 16(1), 97–117.
- Sheng, X., & Zhang, X. (2018). Fuzzy adaptive hybrid impedance control for mirror milling system. *Mechatronics*, 53, 20–27.
- Smith, C., Karayiannidis, Y., Nalpanitidis, L., et al. (2012). Dual arm manipulation—A survey. *Robotics and Autonomous Systems*, 60(10), 1340–1353.
- Sun, P., Song, X., Song, S., et al. (2023). Composite adaptive finite-time fuzzy control for switched nonlinear systems with preassigned performance. *International Journal of Adaptive Control and Signal Processing*, 37(3), 771–789.
- Tao, H., Qiu, J., Chen, Y., et al. (2023). Unsupervised cross-domain rolling bearing fault diagnosis based on time-frequency information fusion. *Journal of the Franklin Institute*, 360(2), 1454–1477.
- Tuan, L. A., Joo, Y. H., Tien, L. Q., et al. (2017). Adaptive neural network second-order sliding mode control of dual arm robots. *International Journal of Control Automation & Systems*, 15(6), 1–9.
- Wahballa, H., Duan, J., & Dai, Z. (2022). Constant force tracking using online stiffness and reverse damping force of variable impedance controller for robotic polishing. *International Journal of Advanced Manufacturing Technology*, 121(9–10), 5855–5872.

- Yan, L., Mu, Z., Xu, W., et al. (2016). Coordinated compliance control of dual-arm robot for payload manipulation: Master-slave and shared force control. In *IEEE/RSJ international conference on intelligent robots and systems* (pp. 2697–2702). IEEE.
- Zekri, M., Sadri, S., & Sheikholeslam, F. (2008). Adaptive fuzzy wavelet network control design for nonlinear systems. *Fuzzy Sets and Systems*, 159(20), 2668–2695.
- Zhai, A., Zhang, H., Wang, J., et al. (2022). Adaptive neural synchronized impedance control for cooperative manipulators processing under uncertain environments. *Robotics and Computer-Integrated Manufacturing*, 75, Article 102291.
- Zhang, Y., Cheng, L., Cao, R., et al. (2023). A neural network-based framework for variable impedance skills learning from demonstrations. *Robotics and Autonomous Systems*, 160, Article 104312.
- Zhang, X., & Khamesee, M. B. (2017). Adaptive force tracking control of a magnetically navigated microbot in uncertain environment. *IEEE/ASME Transactions on Mechatronics*, 22(4), 1644–1651.
- Zhang, X., Sun, T., & Deng, D. (2020). Neural approximation-based adaptive variable impedance control of robots. *Transactions of the Institute of Measurement and Control*, 42(13), 2589–2598.
- Zhao, X., Tao, B., & Qian, L. (2020). Asymmetrical nonlinear impedance control for dual robotic machining of thin-walled workpieces. *Robotics and Computer-Integrated Manufacturing*, 63, Article 101889.
- Zhou, C., Tao, H., Chen, Y., et al. (2022). Robust point-to-point iterative learning control for constrained systems: A minimum energy approach. *International Journal of Robust and Nonlinear Control*, 32(18), 10139–10161.